Northumbria Research Link

Citation: Khalifa, H., El-Safty, S.A., Reda, A., Elmarakbi, Ahmed, Metawa, H. and Shenashen, M.A. (2020) Multifaceted geometric 3D mesopolytope cathodes and its directional transport gates for superscalable LIB models. Applied Materials Today, 19. p. 100590. ISSN 2352-9407

Published by: Elsevier

URL: https://doi.org/10.1016/j.apmt.2020.100590 <https://doi.org/10.1016/j.apmt.2020.100590>

This version was downloaded from Northumbria Research Link: http://nrl.northumbria.ac.uk/id/eprint/43857/

Northumbria University has developed Northumbria Research Link (NRL) to enable users to access the University's research output. Copyright © and moral rights for items on NRL are retained by the individual author(s) and/or other copyright owners. Single copies of full items can be reproduced, displayed or performed, and given to third parties in any format or medium for personal research or study, educational, or not-for-profit purposes without prior permission or charge, provided the authors, title and full bibliographic details are given, as well as a hyperlink and/or URL to the original metadata page. The content must not be changed in any way. Full items must not be sold commercially in any format or medium without formal permission of the copyright holder. The full policy is available online: http://nrl.northumbria.ac.uk/policies.html

This document may differ from the final, published version of the research and has been made available online in accordance with publisher policies. To read and/or cite from the published version of the research, please visit the publisher's website (a subscription may be required.)

Northumbria University NEWCASTLE

CUSTOMER SERVICE EXCELLENCE CSE UniversityLibrary

Multifaceted geometric 3D mesopolytope cathodes and its directional transport gates for superscalable LIB models

H. Khalifa, [a] S.A. El-Safty,*[a] A. Reda, [a] M.A. Shenashen, [a] A. Elmarakbi,[b] and H. Metawa, [a]

[a.] National Institute for Materials Science (NIMS), Sengen 1-2-1, Tsukuba, Ibaraki 305-0047, Japan.

[b.] Department of Mechanical & Construction Engineering, Faculty of Engineering and Environment, Northumbria University, Newcastle upon Tyne, NE1 8ST, UK.

E-mail: sherif.elsafty@nims.go.jp

Webpage: https://samurai.nims.go.jp/profiles/sherif_elsafty

Abstract

In this study, we comprehensively describe the hotkeys of polytope geometrics in terms of heterogeneous and high-index components, surface mobility sites, and hollowness and meso-grooves in potential buildup lithium-ion battery (LIB) designs. We have been fabricated superscalable half-, full-, and large-modulated LIB models by using one dimensional nanorod-like capsules of TiO_2@nanocarbon shells (1D-TO@C) as anodes and a diverse range of multifaceted exposure mesopolytopes based 3D-$LiFePO_4$@C (3D-LFPO@C) geometrics as cathodes. Large-scale, multi-functional 3D-LFPO@C polytope cathodes can tailor function of variable LIB model geometrics with a wide range of charging/discharging cycles and excellent energy density. The integration of mesopolytope 3D-LFPO@C cathode and sustainable capsule1D-TO@C anode enables fabrication of superscalable LIB-CR2032 coin-cell models. Our powerful, full-scale LIB-CR2032-coin cell models are attained Coulombic performance efficacy of ~99.89%, discharge capacity of 93.4% after 2000 cycles, and high specific energy density ≈ 186.98 $Wh.kg^{-1}$, which overrides the requirement for long-driving range of electric vehicles (EVs). Our finding also indicates that the large-scale pouch LIB model designed with dense packing of LIB-CR2032 coin-cells is technically the first polytope LIB-model that fulfilled the energy storage and tradeoff requirements for EVs.

Keywords: Superscalable LIBs; mesopolytopes; high-index surface facets, CR2032-coin LIB cells, time-scale life cycles, energy density.

Introduction

The growing energy crisis is one of the foremost challenges confronting the substantial development in 21st century. The development of environmentally friendly and sustainable energy sources is essential to fulfill the growing need for energy in modern society, and to address the emerging environmental concerns [1]. As a superior reversible energy storage device, rechargeable LIBs are extremely advanced, environmentally clean, and serve as sustainable energy power for many electronic devices [2]. However, their applications have limitations due to their high capital cost and safety problems [1, 3]. Therefore, the electrode fabrication of cathodic/anodic promising candidates is needed for substantial LIB safety and for maintaining high energy density. In this context, fabrication of positive cathode electrode using lithium iron phosphate ($LiFePO_4$, LFPO) has shown a wide range of attention because of its good structural stability, high safety, environment-friendliness, and relative affordability [4, 5]. LFPO has shown theoretically a discharge capacity of 170 mAh g^{-1} and stable voltage plateau around 3.5 V. Despite these characteristics, LFPO cathodes have low tapped density, poor surface conductivity and rate capability, and slow electron/Li^+-ion diffusion at LFPO/$FePO_4$ surface interfaces [5-9]. Such cathodic feature makes its LIB design difficult in large-scale utilization of EVs. Thus, considerable efforts associated with LIB development in terms of the electrode material fabrication have been devoted to provide hybrid nano-/micro-structure electrodes for unique electrochemical performances [3,10, 11]. Various synthesis methodologies of LFPO cathode nano-/micro-structures were used to control its morphological size and shape [3, 12], conductively-active heterogeneous sites [13], and framework composites with other supervalent metals [14-16]. The surface heterogeneity of LFPO composite was improved by decoration of its surface by highly-conductive nanocarbon (nano-C) for high performance LIBs [16- 18]. The geometric control of LFPO with high-index facets, polytope-structure, and multidiffusive open surface sites would become of particular interests for fabrication of variable cathode LIB-electrodes.

Multiple techniques, such as sol–gel, hydrothermal, solvothermal, emulsion drying, co-precipitation, and solid-solid interaction have been used to fabricate a diverse range of LFPO architects [19-25]. Compared with ordinary synthesis approaches, hydrothermal synthesis was used commonly to easily controlled LFPO size, shape and surface reactivity [18, 20]. Recently, LFPO super-architects have been fabricated to enhance the electron/Li^+-ion diffusivity, specific capacity, and rate reversibility and capability [26-28]. In the view of atomic-scale arrangements, the LFPO crystal structure is a key for improving the Li^+ ion kinetics during the lithiation/delithiation process of LIBs [28]. In the ultimate goal of long-term LIB-EVs-driving range with excellent power, control fabrication of cathode/anode electrodes with ordering geometrics, heterogeneous and high-index components, and modular building blocks is curial to manipulate the LIB models. Therefore, the fabrication of polytope LFPO cathode electrodes with multifaceted exposures, a bundle of surface vacancies, cavities and windows may offer large-scale surface loads and diffusion of electrons/Li^+ ions. The desired LFPO crystal orientation with specified high-index facets may improve the electron mobility and conductivity, surface motivation capability, and Li^+ ion diffusion at interfaces, leading to high LIB–EV performances [28, 29].

As large-scale modulation of low procurement cost LIB-EVs, nano-sizable transitional metal oxides (MOs) are promising anode materials for LIBs [30]. Among these MOs, titanium dioxide structures with anatase-TiO_2 phase (TO) are likely to be electro-active hosts for Li^+ ion-insertion [21, 31]. Furthermore, TO features included high safety, affordability, non- poisonous effects, low polarization, and highly reversible property were led to fabricate a negative electrode with excellent charge/discharge cyclic stability [32-35]. The flexibility in the structural phase transition of TO from I41/amd-tetragonal orientation into lithium-rich $Li_{0.5}TiO_2$ Imma-orthorhombic geometrics was supposed to be responsible for long-range reversible systems [36- 39]. The spontaneous conversion of Li-poor $Li_{0.01}$TO phase into Li-rich $Li_{0.5}$TO offered electrode structure with high flexibility and reversibility. Further development of reversible structural TO anode will reduce the LIB manufacture burden and procurement costs. As an anodic electrode modulated LIB for high energy density, the primary key of one-dimensional **(**1D)-TO pipe-like tubes may open abundant Li^+/electron gate-in-transports and occupants, and hops-built-in anode electrodes. The 1D-capsule coated nanocarbon (1D-TO@C) electrode array may provide uniform accommodation/storage pockets, and geometrical models for massive charge/discharge cycles of LIBs.

Likely, the current study shows the superscalable modulation of half-, full-, and large-scale mesopolytope 3D-LFPO@C cathode // capsule 1D-TO@C anode LIB-CR2032 coin-cell LIB-models. The heterogeneous high-index 3D-LFPO@C polytopes such as 16-faceted exposure polyhedron (SFP@C), octahedron simplex (OS@C), rhombus platelet (RP@C), parallelepiped complex object (PC@C), and convex complex (CC@C) cathodes are key candidates for a new generation of variable polytope-LIB model geometrics. Our remarkable half-cell polytope 3D-SFP@C cathode electrode exhibits outstanding discharge capacities of 168.72, 158.62, and 135.34 mAh g^{-1} at C-rate of 0.1, 1, and 20 C, respectively, and at potential range of 2–4.3 V (vs. Li^+/Li). The heterogeneous polytope SFP@C// capsule 1D-TO@C full-scale LIB model sets attain 93.4% of its 1st discharge capacity (mAh g^{-1}) after 2000 cycles, Coulombic performance efficacy of ~99.89% at 0.1C rate, and high specific energy density 186.98 Wh kg^{-1}. Significantly, attempts for large-scale modulation have been carried out through a dense packing in a collar fashion of multiple LIB-CR2032-coin cells, enabling a design of pouch LIB model. This pouch LIB-model offers superb rate capability, charge/discharge cycle stability, high areal discharge capacities and remarkable gravimetric and volumetric energy and tap densities for LIB-EV applications.

Experimental

Design of 1D-TO@C capsule and 3D-LFPO@C polytope materials

Various combinations of multi-functional heterogeneous high-index mesopolytope LFPO materials with 16-faceted exposure polyhedron (SFP@C), octahedron simplex (OS@C), rhombus platelet (RP@C), parallelepiped complex object (PC@C), and convex complex (CC@C) geometrics are fabricated and used for fabrication of cathodes. The 1D-TO nanorod capsules are fabricated simple synthesis condition and used as anodes. All cathode materials are fabricated under control of Li-anion sources (see supporting information S1). In addition, the carbonization process of the 1D-TO capsule and 3D-LFPO polytope materials was simply applied to cover their surfaces by nano-carbon-shells with 3-5 nm layer dressers. The carbonization methodology of 3D-LFPO@C polytopes (cathodes) and 1D-TO@C capsules (anodes) was carried out by using microwave radiation technique (see supporting information S1-S12).

Formulated components of mesopolytope 3D-LFPO@C and 1D-TO@C capsules in P- and N-electrodes and LIB models

The half-cell anodic-electrode batteries is fabricated by loading special amount of 1D TiO_2@C (1D-TO@C) nanorod-like capsule architects into 8 µm-cupper (Cu) foils (i.e., negative (N) electrodes). The half-cell cathodic electrode batteries are successfully designed by loading of specific amounts of multi-functional 3D-LFPO@C polytopes such as 16-faceted exposure polyhedron (SFP@C), octahedron simplex (OS@C), rhombus platelet (RP@C), parallelepiped complex object (PC@C), and convex complex (CC@C) into 10µm-aluminum (Al) foils (i.e., positive (P) electrodes). The integration of heterogeneous mesopolytope 3D-LFPO@C cathodic and capsule 1D-TO@C anodic electrodes in coin-shaped like discs leads to fabricate CR2032-coin LIBs. The proposed full-scale LIB-model design components are formulated by using heterogeneous mesopolytope 3D-LFPO@C cathode / capsule 1D-TO@C anode geometrics. We have carried out a set of electrochemical experiments to prove the potential formulation of variable half-, and full-scale LIBs. Our measurement sets are built to study the effectiveness of key 3D-LFPO@C structures in the high-performance storage battery as follows: (i) the formation of surface meso-grooves, caves, hollowness-like nests in the core of polytopes; (ii) the well-ordered orientations of 6-, 8-, and 16-exposed active surface sites; (iii) the regular polytope single-crystal-structure with heterogeneous high-index, and homeomorphic facets ; (iv) single crystal defects along kinks, vertices, and ridges; and (v) the well-dispersed decoration of with uniform and thin shells of nano-C layers.

Technical and mechanical key control of half- and full-cell polytope CR2032-coin LIB formulations

A setting of effective half- and full-cell LIBs is designed for purposing the low-cost manufacturing, ever-decreasing discharge timescale yet maintaining high-energy density. Half-scale capsule 1D-TO@C anode and mesopolytope 3D-LFPO@C cathode LIBs are explored by using CR2032-coin cells (see supporting information). For high electrochemical performances and improving safety issues of half- and full-scale LIBs, the technical and mechanical key controls of coin cell LIB formulations are essential, according to the following consequence steps:

First, we used a disc cutter to form well-defined circular electrodes and separator films with specific diameters as follows: (i) a 16 mm for Li-foils can be used as counter and reference electrodes, (ii) 16 mm Al- and Cu-foils are used as working electrodes, and (iii) a 20 mm Celgard 2400TM membrane can be used as microporous polymer separator. **Second,** the electrolyte used with half- and full-CR2032-coin cells can be fabricated as follows; a 1 M conductive lithium hexafluoro-phosphate ($LiPF_6$) solution is dissolved in a mixture of ($C_5H_{10}O_3$) diethyl carbonate / ($(CH_2O)_2CO$) ethylene carbonate (1:1 v/v). The potential function of highly conductive electrolyte ($LiPF_6$/ $C_5H_{10}O_3$/$(CH_2O)_2CO$) leads to improve the optimization of the electrochemical performance and diminishes the loss of reversible capacity of half- and full-CR2032-coin LIB cells. **Third**, the active 1D-TO@C capsule anode and 3D-LFPO@C polytope (i.e., SFP@C, OS@C, RP@C, PC@C and CC@C) cathode materials are separately mixed with a component of carbon-black/polyvinylidene fluoride (PVDF) with mass equivalent ratios of 75: 15: 10, respectively. To this heterogeneous mixture, a rational amount of N-methyl-2-pyrrolidone (NMP) is added and stirred for 1 h to fabricate the active material slurries. consequence fabrication steps based on we fabricate the mesopolytope 3D-LFPO@C and capsule 1D-TO@C in P- and N-working electrodes by using the immobilization techniques. The active slurries of mesopolytope 3D-LFPO@C and capsule 1D-TO@C (i.e., cathodic and anodic materials) are incorporated into 10 μm-aluminum (Al) and 8 μm-cupper (Cu) foils, respectively. The functional anode/cathode disc-like films are then dried at 80 °C in a vacuum oven for 12 h. The resultant mesopolytope 3D-LFPO@C-incorporated Al-foils and capsule 1D-TO@C-incorporated Cu-foils are used as working positive (P) and negative (N) electrodes, respectively. Note that the loading amount (i.e., mass/electrode area) of the active1D-TO@C capsule anode or 3D-LFPO@C polytope cathode materials into 8 μm-Cu or 8 μm-Al foils is 6.63 or 13.14 mg/cm^{-2}, as reported in supporting information S1.

Fifth, the prepared components of the coin-cell batteries are left for 24 hours prior any electrochemical measurements. The dryness process is applied to enhance the component stability onto electrodes and to reach to the equilibration state between total electrolyte-intake solutions and

N- or P- solid surface electrodes. The dried working electrodes based mesopolytope 3D-LFPO@C-incorporated Al-foils and capsule 1D-TO@C-incorporated Cu-foils (P- and N-electrodes) are compressed between twin rollers in order to achieve the following fabrication keys of cathode and anode LIBs:

i. the dense packing materials onto 10 µm-Al and 8 µm-Cu foil surface interfaces,

ii. reduction of the voids and spaces along the overall mesopolytope cathode/ capsule anode electrode film surfaces for high electric conductivity, and

iii. to strengthen the diffusivity and surface contact binding between the active mesopolytope cathodic and capsule anodic materials and the 10 µm-Al and 8 µm-Cu foil electrode collectors, respectively.

In the regard of environmentally-friendly LIB packaging, the dense packing of LIB coin-cell components, electrolytes and electrodes becomes compulsory to improve LIBs with safety betterment. However, the safe-type LIBs should also attain the ever-decreasing discharge timescales and high-energy density that required for longest LIB-EVs driving range. The compression of the CR20XX series coin cells is occurred by using crimper machine. The compressing process is carried out inside glove box under argon gas for further measurements and tests (see supporting information S1-S13).

The rational controls of polytope SEP@C (P-electrode) and capsule 1D-TO@C (N-electrode) mass ratios (.i.e., the balancing $(P/N)_{Cap}$ ratio ≈1.0: 1.07-1.14) that loaded onto 10 µm-Al-foils and 8 µm-Cu-foils are significant for full-cell LIB safety concerns, and sustainability of its performance against long-period cycles. The specific $(P:N)_{Cap}$ ratio with optimal ≈1.0: 1.09 leads to optimal tradeoff LIB models, in which provide better cell battery safety with preserving an excellent energy density, see supporting information S13.

Ordered sets of mesopolytope SFP@C // capsule 1D-TO@C CR2032-coin cells in pouch LIB models

The ever increasing demands of large scale LIB pouch models in EVs, control over the required high areal discharge capacities and remarkable gravimetric and volumetric energy and tap densities are urgently needed. For example, the tap density is mainly influenced by the heterogeneous cathode/anode materials and their high-index components, active surface mobility sites, multifaceted exposures and the distribution of powder particles along the electrode surfaces. Our experimental finding of polytope electrode design indicates that the dense packing SFP@C-Al-foil P-electrodes show higher tap density values of ~1.55 g cm^{-3} than that of other 3D-LFPO@C-Al-foil electrodes. Therefore, we used mesopolytope SFP@C cathode as P-electrode in the full design of polytope CR2032 coin-cell LIB-models.

Aiming to multi-scale implementations, ordered sets of multiple rolls of coin cells are packed-up in a collar fashion to form pouch LIB models. In this pouch design, the working electrode components are formulated with stacked-layers of 1D-TO@C nanorod-like capsule (anode), and 3D-LFPO@C mesopolytope (cathode). To practically-designed pouch-type LIBs, a set of stacked layers of mesopolytope SFP@C cathode P-electrode // capsule 1D-TO@C anode N-electrode that oriented in full-scale LIB-CR2032-coin-cell components (Figure S13). The stacking layers of mesopolytope SEP@C cathode P-electrode // capsule 1D-TO@C anode N-electrode are arranged layer-by-layer with 6-//5-layer numbers, respectively. The resultant 6-layers of mesopolytope SFP@C-incorporated 10 μm-Al-foils and 5-layers of capsule 1D-TO@C-incorporated 8 μm-Cu-foils are oriented consecutively in 12 sides, respectively; see supporting information S13, S14. According to these ordered layer sets, the mass stacking of mesopolytope SEP@C cathode P-electrode // capsule

1D-TO@C anode N-electrode is 13.14 and 6.63 mg/cm^2, respectively. Our finding indicates that the areal discharge capacity of the stacking mesopolytope SEP@C cathode P-electrode // capsule 1D-TO@C anode N-electrode is 1.144 and 1.145 Ah/cm^2, respectively. The experimental fabrication sets are studied for the building of large-scale mesopolytope SFP@C // capsule 1D-TO@C LIB-CR2032 coin-cell models, see supporting information (S1-S16)

Results and Discussion

Fabrication of mesopolytope 3D-LFPO@C and capsule 1D-TO@C as P- and N-electrode materials

In terms of anode/cathode electrode material costs, the proposed electrode battery model system is based on the simple fabrications of following (i) high-index mesopolytope LFPO cathode materials, (ii) 1D-TO nanorod capsule-like anode materials, (iii) multi-functional heterogeneous anode/cathode materials via coating of nano-carbon layers onto their outer surfaces, and (iv) mesopolytope 3D-LFPO@C and 1D-TO@C capsules in P- and N-electrodes, respectively. Control engineering of unique geometrics, nanoscale vaccinates and multiple crystal facets creates 1D and 3D open-end directional gates along 1D-TO@C nanorod capsules and superscalable mesopolytope 3D-LFPO@C electrode surfaces, respectively. The incorporation of these heterogeneous mesopolytope 3D-LFPO@C cathode and capsule 1D-TO@C anode onto 10 µm-Al and 8 µm-Cu foils would lead to fabricate spatial P- and N-electrodes. The electrode surface topologies with multidirectional gates, heterogeneous high-index components, active mobility sites, meso-grooves, and multifaceted polytope exposures are affected the anode/cathode potential. The architectural geometrics of P- and N-electrodes affect the diffusion capability and electrochemical reactivity of their potential half- and full-scale LIBs.

3D-LFPO polytope-modified nanocarbon architectures, such as high-index, sixteen (16)-faceted polyhedron-crystal-structure SFP@C, octahedron simplex (OS@C), rhombus platelet (RP@C), parallelepiped complex object (PC@C), and convex complex (CC@C) polytopes, are used as cathodes in half-, full-, and large-scale LIB models. These cathode materials are synthesized by varying the lithium-compound sources (such as Li-acetate, -chloride, -hydroxide monohydrate, -nitrate, and -carbonate, respectively). In addition, a control over seed (particle) growth time at high temperature treatment is necessary (see supporting information S1). The growth mechanism of LFPO particle crystals leads to tailor various 3D geometric architects. Typical polytope mechanism can be achieved through (i) nucleation-growth building agent (such as Li-anions) and (ii) auxiliary structure reagent (such as ethylene glycol/ ethanol mixture). Both key synthesis factors can significantly reduce nucleation surface curvature and suppress the $Fe^{3+/}Fe^{2+}$ active surface, thereby resulting in thermodynamically formulated variable 3D-LFPO geometries and simplex, convex, and homeomorphic polytopes. In this Li-anion-assisted polytope nucleation-growth, the alteration from the high potential reduction of Li-anion precursors (such as Li-carbonate and -nitrate) to low potential reducers (such as Li- hydroxide monohydrate, -acetate dihydrate, and -chloride) can control the changes of the polytope model geometrics from a convex complex structure (CC), which passes through a parallelepiped complex structure (PC), rhombus platelets (RP), and octahedron structure (OS), to a high-index 16-faceted polyhedron structure (SFP), respectively. The low reducing potential power of the Li-anion precursor would likely provide sufficient time for the effective growth and then development of high-index facet building units, such as SFP polytopes. By contrast, Li-anion precursors of high-potential reducing agents accelerate reaction kinetics, thereby leading to a formation of convex complex CC structures. Furthermore, the open-end tubular structure of 1D-TO nanorod-like capsule can be controlled under high-temperature treatment of titanium (IV) ethoxide $Ti(OC_2H_5)_4$ composite domains.

To tailor the surface heterogeneity, electronic conductivity and geometric stability of 1D-TO capsules and 3D-LFPO mesopolytopes (such as SFP, OS, RP, PC, and CC structures), sustainable ~5 nm C-shell dot-dressers are coated the outer surface layers of both anode and cathode materials without changes in the structural ordering, and atomic scale geometrics of resultant 1D-TO@C anode and polytope 3D-LFPO@C cathode materials (see supporting information S2-S9). In anode/cathode electrode designs, the decoration of 1D-TO capsule and LFPO polytope with nano-C-dot as mat layers coverage the 1D-TO capsule and LFPO polytope electrodes would enhance anisotropic heterogeneity, reactive mobility, electronic conductivity of their surfaces. These heterogeneous mesopolytope SFP@C (cathode) and capsule 1D-TO@C (anode) electrodes can be promising for next-generation LIB-EVs due to its multiple 1D and 3D directional transport gates, diffusion dynamics, and structural stability. The buildup of heterogeneous 1D-TO@C anodes and polytope 3D-LFPO@C cathodes in half-, full-, and large-scale LIB models are promising hybrid designs for higher gravimetric and volumetric energy and tap densities, rate capability, and areal discharge capacities than that of non-coated carbon parent capsule (anode) or polytope (cathode) electrodes-modulated LIBs (i.e., TO-anode// LFPO-cathode). The electrode stability inside the integral LIB-CR2032-coin cells will maintain the heavily-loaded occupants of Li^+-ions and continuous electron/ Li^+ ion movements along the anode/cathode surfaces, even after a massive of lithiation/delithiation processes, leading to optimal requirements of an ageless reachable battery.

Fig. 1

Geometrical orientations of 3D-LFPO@C and capsule 1D-TO@C along P-, and N-electrodes

Nanoscale geometric structures of 1D-TO@C nanorod-like capsules (anode) and 3D-LFPO@C polytope cathodes were examined by using microscopic analyses patterns of (FE-SEM) field emission scanning electron microscopy, (EDX) energy-dispersive X-ray spectroscopy, (EM) elemental mapping, (ED) electron diffraction, and (HR-TEM) high-resolution transmission electron microscopy (Figs. 1, 2, and S2–S5). In general, our findings show evidence of control engineering of well-ordered geometric shapes, high-index components, active surface mobility sites, multifaceted polytopes, and 1D and 3D directional gates throughout the hollowness and meso-grooves, and one-open-end capsules. For example, Figs. 1(A–D) provide a schematic configuration of SFP@C polyhedron with multifaceted exposure {101} and {105} facets. This mesopolytope SFP@C consists of typically-truncated shape at medium of tetragonal bipyramids with exposed {101} and {001} facets. In addition, two pudgy tetragonal pyramids with dominantly exposed high-index {105} facets are oriented on opposite sides of the truncated tetragonal bipyramids. Figure 1D shows the EDX and EM analyses of SFP@C polyhedron components of O: Fe: P: C with percentage ratios of 56.8: 21.7: 19.6: 1.9 %, respectively. Figure 1 (A–C) shows a clear evidence of the formation of (i) 3D directional pathways along the interior hollowness and meso-grooves of SFP@C, and (ii) the multi-diffusive accommodation storage through nanogrooves, cages, and geodes. These mesopolytope geometric structures, and surface topographies enable multiple directional gates and pathways, a decrease in the distance of electron transport, and multidiffusible Li^+ ions. Figures 1 (E–H) clearly illustrate the formation of large-scale polytope geometrics with heterogeneous high-index, homeomorphic simple and complex shapes, including OS@C, RP@C, PC@C, and CC@C morphologies, as clearly illustrated in supporting information, Figs. S2–S5. These variable model geometrics, surface heterogeneities, and multi-facets with 8- and 6-exposure sites of mesopolytopes are used to tailor the function of cathode electrodes in the fabrication of half-, full-, and large-scale LIB models.

The atomic-scale ordering structures of 3D-cathodic mesopolytope SFP@C, OS@C, RP@C, PC@C, and CC@C architectures are evidence from HR-TEM patterns (see Figs. 1(I–L), S2(D–F), S3(E–G), S4(D–F), and S5(E–G), respectively). All mesopolytope cathodic SFP@C, OS@C, RP@C, PC@C, and CC@C samples show crystal planes with interatomic d-spacing values of (0.39, 0.98), (0.39, 0.98), (0.41, 1.01), (0.39, 1.01), and (0.39, 1.03) nm, in agreement with (001) and (100) planes of orthorhombic 3D-LFPO mesocrystals, respectively. The ED pattern images of single crystals of SFP@C, OS@C, RP@C, PC@C, and CC@C geometric blocks are shown in Figs. 1(L), S2(F), S3(G), S4(F), and S5(G), respectively. Our microscopic analysis reveals that the exposure [010] ac-plane sites are predominant and low surface energy sites of such 3D-LFPO mesopolytopes. These nanoscale geometric mesopolytopes enable suitable accommodation objects of electrons/Li^+ ions during lithiation/delithiation processes. The crystal growth orientations of all heterogeneous mesopolytope cathode composites are prominently preferable along the [010] plane, thereby leading to high-rate capability [18,28,40, 41]. The lattice patterns in Figs. 1(K), S2(E), S3(F), S4(E), and S5(F) show clear, thin, and smooth 4–5 nm layers of C-shell dressers at the surface edges, vertices, and faces of mesopolytope cathodes. The well-ordered, thermally stable, and sustainable coating layers by C-shells along these mesopolytope structures were characterized via thermogravimetric analysis, Raman spectra, X-ray photoelectron spectrometry, and Fourier transform infrared spectra, as shown in the supporting information (Figs. S6–S9).

Fig. 2

Figure 2 shows 1D object of TO@C nanorod-like capsules (anode). The capsules have open-end channel-like gates and an abundance of mesopores along surface frameworks, as evidence from FE-SEM, EDX, ED, EM, and HR-TEM microscopic analyses. Figures 2(a–b) verify the interior/exterior ordering of nano-C-dot layers organized along the entire anatase 1D-TiO_2 nanorods, thereby leading to from sustainable 1D-TO@C capsules. Figure 2(C) shows the 3D projections of anodic capsules with 1D channel that exhibits open-end hole-like mouth in its both sides. Well-ordered coverage layers of nano-C dots are oriented along the nanorod channels, leading to create multiple directional gates, active surface mobility sites, and meso-grooves. Well-dispersed element components of O, Ti, and C with amount ratios of 70.3:28.4:1.3, respectively, are characterized the 1D-TO@C capsule anode (Figure 2d). HR-TEM and ED microscopic patterns (Fig. 2e,f) show evidence of the formation of (i) crystal structure oriented along [101] plane direction, (ii) ~3 nm shell-layered dressers of nano-C-dot along all the TO nanorod surfaces, and (iii) 1D open-end directional gate of 1D-TO@C capsules oriented in anodic electrode.

Surface characteristics of mesopolytope 3D-LFPO@C and capsule 1D-TO@C geometrics

Figures 3(a) and S10 show the X-ray diffraction patterns (XRD) of the 3D-LFPO@C cathode and 1D-TO@C anode structures. Figure 3a exhibits the XRD peaks and profiles (lattice parameters of a = 9.962 Å, b = 6.080 Å, and c = 4.678 Å, in addition to the unit volume of 286.95 Å^3) of 3D-LFPO orthorhombic olivine with Pnma symmetry group (JCPDS Card No. 83-2092) [28,42]. All SFP@C, OS@C, RP@C, PC@C, and CC@C geometric structures showed structural stability 3D-$LiFePO_4$@C without any competitive phase formations such as Li_3PO_4, $Li_3Fe_2(PO_4)_3$, conductive FeP, and $Li_4P_2O_7$. The representative 3D-LFPO [010]-orthorhombic olivine structure shows evidence of the atomic-scale arrangements along its surface direction (Fig. 3b). The 3D-LFPO@C crystal orientation with a highly exposed *a-c* plane has optimal surface energy for (i) fast electron/Li^+-ion diffusion dynamics and (ii) superb kinetics of lithiation and delithiation. Figure S10 exhibits the XRD peaks and profiles (lattice parameter of a= 3.789 Å, b= 3.789 Å, and c = 9.489 Å) of anatase 1D-TO@C tetragonal structure with the $I4_1$/amd symmetry group (JCPDS 21-1272). The crystal structure stability of 1D-TO@C anode renders the regularity of the electron/Li^+-ion movements along axial and frontal crystal planes.

Fig. 3

The textural surface parameters of mesopolytope 3D-LFPO@C and capsule 1D-TO@C geometrics such as dynamic arrangement of space holes, mesogrooves, and surface coverage areas enable the formulation of missive diffusion gateways for fast charge–discharge capability rates of LIBs [43-47]. We have measured the N_2 isotherms of mesopolytope cathodes to determine the specific surface areas (S_{BET} m^2/g) of mesoporous polytope structures (Figs. 3[c,d). The N_2 isotherms featured a type IV with H_2 hysteresis loop for all tested SFP@C, OS@C, RP@C, PC@C, and CC@C cathode samples, indicating the formation of mesocage caves and high surface coverages of the entire mesopolytope structures. The mesopolytope-type orientation, variable model geometrics, and multifaceted surfaces affected the key factors of textural surface parameters. For example, the (S_{BET} m^2/g) values decreased in this order: SFP > OS > RP > PC > CC geometric blocks. The calculated BET surface areas are 346.8, 217.2, 107.7, 84.1, and 15.5 $m^2.g^{-1}$, and the corresponding pore size diameters are 11.1, 12.1, 12.0, 14.1, and 19.0 nm for SFP@C, OS@C, RP@C, PC@C, and CC@C cathode samples, respectively. Among all mesopolytope structures, the SFP@C cathode surface electrodes are candidate for long-term storage cycles, continuous rate capability and charging/discharging stability, and excellent energy density.

Key fabrication profiles of half-, full-, and large-scale LIB-CR2032 coin-cell models

Together, for a new generation of heterogeneous half-, full-, and large-scale LIB models, the unique structures of the cathodic mesopolytope 3D-LFPO@C morphologies of SFP@C, OS@C, RP@C, PC@C, and CC@C geometrics prove the potential cathode candidate in the integral and outstanding LIBs. In these powerful LIB models, multiple mass transports along the 1D open-end directional gates of 1D-TO@C nanorod capsules (anode) and 3D superscalable mesopolytope crystal facets (cathode) mainly depends on the geometric unit blocks of polytope structures, hollowness grooves, and multifaceted exposures. Along all used 3D-LFPO@2C polytope cathodes designed LIB models, the high-index exposure sites and surface anisotropicity, heterogeneity and conductivity of SFP@C geometrics may produce extra-ordinary transportation, diffusion dynamics, and storage accommodation of electrons/Li$^+$ ions. The SFP@C mesopolytope may be considered a demanded cathode to meet the requirements of high energy density and long-term rate cycling of LIB-EVs.

The key fabrication points of half-, full-, and large-scale mesopolytope SFP@C // capsule 1D-TO@C LIB-CR2032 coin-cell models are as follows: (i) formation of grooves and hollowness-like geode caves in the core, (ii) distribution of highly dense exposure active surface sites of multiple polygon tetragonal and triangular facet components, and (iii) surface heterogeneity, and conductivity of cathode/anode electrodes, (iv) flexible mobility sites along accommodated vicinities, edges, incidence focal cages, vertices, and terraces for boosting the electron/Li$^+$-ion diffusivity, and (v) movement of electrons/Li$^+$ ions along axial, and frontal crystal planes for remarkable specific cycle capacity, and rate reversibility and capability. To gain a full understanding of these hotkeys in the buildup of large-scale LIBs, we intensively studied the electrochemical performance of variable cathode model geometrics, such as homeomorphic SFP@C, OS@C, RP@C, PC@C, and CC@C mesopolytopes designed half-cell cathode LIBs (see Figures 4-6). The electrochemical performance of half-scale capsule 1D-TO@C LIB-anode model is also investigated (see Figure S12). Remarkably, superscalable, full-, and large-scale mesopolytope SFP@C// capsule 1D-TO@C LIB-CR2032 coin-cells packed in pouch-type models are technically the first studies of polytope LIB-geometrics.

Half-cells: mesopolytope 3D-LFPO@C half-scale cathode LIB-CR2032 coin-cells

The electrochemical performances of mesopolytope 3D-LFPO@C half-scale cathode LIB-CR2032 coin-cells based on variable homeomorphic electrode surfaces such as SFP@C, OS@C, RP@C, PC@C, and CC@C mesopolytopes are designed and measured, as shown in Figures. 4–6.

Fig. 4

The cyclic voltammogram (CV) curves are determined at potential region of 2–4.3 V vs. Li/Li$^+$ and at a sweep rate of 0.1 mV/s for variable homeomorphic cathode electrode surfaces such as SFP@C, OS@C, RP@C, PC@C, and CC@C mesopolytopes (Fig. 4a). The defined reduction/oxidation peaks are observed at 3.28/3.48, 3.23/3.51, 3.17/3.57, 3.23/3.68, 3.10/3.67, and 3.04/3.76 V of mesopolytope SFP@C, OS@C, RP@C, PC@C, and CC@C half-cell cathode electrodes, respectively. The 1st cycle CV curves of mesopolytope SFP@C cathode are recorded at C-rates of 0.1, 0.5, 1, 5, and 10 C/ mVs^{-1} and at potential range of 2–4.3 V vs. Li/Li$^+$ (Fig. 4b). Figure 4b shows that with the increasing in C-rates, (i) the voltage values for oxidation peaks increase, whereas the voltage values for reduction peaks are decreased, and (ii) the current values (mA) for both oxidation/reduction peaks are increased. Figure 4c shows the cyclic stability profiles of the mesopolytope SFP@C cathode with 1st, 2nd, 3rd, 50th, and 100th cycles determined at C-rate of 0.1 mVs^{-1} and at a 2.0 - 4.3 V potential range. The Fe$^{3+/}$Fe^{2+} symmetric and spiculated peak profiles for 3D-LFPO@C with mesopolytope SFP@C cathode are observed at 3.28/3.48 V within 1st, 2nd, 3rd, 50th, and 100th cycles. The similarity in oxidation/reduction peak profiles (i.e., different cycles at one potential range) indicates the excellent reversibility of 3D-LFPO@C with mesopolytope SFP@C cathode. The effective cathode reversibility leads to the facile lithiation (reduction) / delithiation (oxidation) processes at cathode/anode surfaces (i.e., Li$^+$-insertion/ Li$^+$-extraction mechanism), respectively [48]. The considerable overlapping of Fe$^{3+/}$Fe^{2+} symmetric and spiculated peaks in the 1st-100th cycling CV curves is attributed to the excellent charge–discharge process and a high reversible capacity within multiple cycles. Figure 4(d) shows the 1st discharge capacity for mesopolytope 3D-LFPO@C half-scale cathode LIB-CR2032 coin-cells based on variable homeomorphic electrode surfaces such as SFP@C, OS@C, RP@C, PC@C, and CC@C mesopolytopes. The discharge capacity profile (mAh/g) is determined at various C-rates (mV/s) in the range of 0.1–20 C and at potential region of 2.0- 4.3 V vs. Li/Li$^+$. The 1st discharge capacity values at overall scan rates are decreased in this direction: SFP@C >OS@C >RP@C >PC@C >CC@C cathodes along. This result indicates that among all mesopolytopes of SFP@C, OS@C, RP@C, PC@C and CC@C half-cell cathodes, the sixteen-faceted exposure polyhedron (SFP@C) cathode exhibits high cycling stability and discharge capacity at several scan rates in the range of 0.1–20 C.

Fig. 5

Variable 3D-LFPO@C homeomorphic electrode geometrics such as SFP@C, OS@C, RP@C, PC@C, and CC@C mesopolytopes that fabricated with wide range varieties in orientations, multi-facets of 6-, 8-, and 16-exposed sites, and surface heterogeneities and interfaces are significantly affected the performance of half-scale cathode LIB-CR2032 coin-cells (Figure 5A). For example, Figure 5 B show a clear evidence of the key clues of the cathode geometrics such as SFP@C, OS@C, RP@C, PC@C, and CC@C mesopolytopes on the charging/discharging cycles. Figure 5(Ba) exhibits the charge/discharge cycling performance for polytope SFP@C, OS@C, RP@C, PC@C, and CC@C half-cell cathode electrodes at a potential region of 2–4.3 V vs. Li/Li$^+$ at a C-rate of 0.1C (mV/s). As experimental sets, the 3D superscalable polytope 3D-LFPO@C half-cell cathodes are charged to 4.3 V at 0.1 C, and then retained at 4.3 V for 1 h. After that the 3D-LFPO@C cathodes are then discharged to 2.0 V at 0.1 C. Among all half-scale cathode LIB-CR2032 coin-cells, the SFP@C half-cell cathode showed a higher storage capacity compared with all mesopolytope cathodes. For example, the SFP@C cathode shows the highest discharge capacity of 168.72 mAh g^{-1} at 0.1 C-rate. However, the other polytope OS@C, RP@C, PC@C, and CC@C cathodes provide high discharge capacities of 158.9, 147.9, 136.6, and 125.5 mAh g^{-1} at 0.1 C-rate, respectively. Figure 5B-b exhibits typical 1st cycle charge/discharge curves of SFP@C half-scale cathode LIB-CR2032 coin-cells at different sweep C-rates (i.e., 0.1, 0.2, 0.5, 1, 5, 10, and 20 C (mV/s)) over the 2–4.3 V (potential range) vs. Li/Li$^+$. The result reveals that the SFP@C cathode with 16-facets and high-index exposure surfaces, active surface mobility sites, hollowness and meso-grooves, and window gateways exhibits excellent behavior for high discharge capacity (mAh/g) at overall C-rates (i.e., 0.1–20 C range) compared with other polytope half-cell cathodes designed with low-index-facets of 6-, and 8-exposed sites, such as OS@C, RP@C, PC@C, and CC@C mesopolytopes (Figure 5A). Figure 5(B–c) exhibits the charging/discharging capacity profiles and the long-term cycling performance (1^{st}-100^{th} range of cycle numbers) of the high-index exposure sites and 16-facets of SFP@C half-scale cathode LIB-CR2032 coin-cells at a C-rate of 1.0 C. Furthermore, the cycling performance of all half-cell cathode geometrics such as SFP@C, OS@C, RP@C, PC@C, and CC@C mesopolytopes is shown in Figure 5B-d. The SFP@C half-scale cathode LIB-CR2032 coin-cells exhibit superiority in the retention rate of 98.6% of its 1^{st}-cycle discharge capacity after 100 cycles and at 1 C. In turn other half cell cathode geometrics with OS@C, RP@C, PC@C, and CC@C mesopolytopes retain about 97.2%, 96.8%, 94.4%, and 89.5% of their initial discharge capacities after 100 cycles and at 1 C, respectively. These results indicate the cycling sustainability in high discharge capacity over the 100^{th} cycle with high-index exposure sites and 16-facets of SFP@C half-scale cathode LIB-CR2032 coin-cells at a C-rate of 1.0 C compared with other variable cathode model geometrics that have low index 8- or 6-faceted mesopolytopes (Figure 5A). This finding emphasizes that the 3D-mesopolytope SFP@C cathode has excellent electrochemical reversibility during lithiation/delithiation processes.

Further related to the effectiveness of variable 3D LFPO@C cathode model geometrics in the long-period stability of half-scale cathode LIB-CR2032 coin-cells in terms of (i) charging/discharging capacity cycling, and (ii) the capability performance rate is shown in Figure S11a. The cycling capacity performance (1^{st}-100^{th} range of cycle numbers) of polytope SFP@C, OS@C, RP@C, PC@C, and CC@C half-cell cathode electrodes at a potential region of 2–4.3 V vs. Li/Li^+ at C-rates of 0.1, 0.2, 0.5, 1, 2, and 5 C (mV/s). To evaluate the rate capability all half-cell cathode geometrics, the discharge capacities at C-rates of 0.1C-5.0C are back to 0.1C and 10 C, and then followed by returning back to 1.0C and 20 C at 25 °C. We also preform the discharge capacity pattern of all polytope 3D-LFPO@C half-cell cathode electrodes at each C-rate (mV/s) within 10th cycles until reaching to 100th cycles.

Figure S11(a) also shows evidence that specific capacity performance is decreased, whereas the C-rate (mV/s) for all polytope SFP@C, OS@C, RP@C, PC@C, and CC@C half-cell cathode electrodes is gradually increased from 0.1 C to 20C. The 16-faceted SFP@C half-scale cathode LIB-CR2032 coin-cells exhibit long-period cycle stability in terms of a remarkable cycle capacity performance, and an outstanding rate capability at overall C-rates (i.e., 0.1 C-20C range) of over cycle numbers (i.e., 1st-100th range). Our finding indicates that the 16-faceted SFP@C half-scale cathode LIB-CR2032 coin-cells show excellent dischargeable and reversible capacity, approximately of 126.4 mAh g^{-1} at a 20 C sweep rate and after 100th cycles. The discharge capacity of other polytope OS@C, RP@C, PC@C, and CC@C half-cell cathode electrodes is dropped markedly to 103.6, 75.5, 42.3, and 6.5 $mAhg^{-1}$ at a 20 C sweep rate and after 100th cycles during reversible Li^+-inclusion/-exclusion cycling processes.

Figure S11(b) shows evidence of the effectiveness of variable 3D LFPO@C cathode model geometrics in the electrochemical impedance spectroscopy (EIS) results. The Nyquist plots for polytope SFP@C, OS@C, RP@C, PC@C, and CC@C half-cell cathode electrodes are determined (see Figure S11b and its magnification). At high-, and low- frequency regions, all Nyquist graphs of polytope SFP@C, OS@C, RP@C, PC@C, and CC@C half-cell cathode electrodes show sizable semicircle curvatures, and diagonal lines, respectively. On the basis of EIS result and its equivalent circuit (see supporting information S1 and Fig. S11-b), the resistance of the charge (–ve/+ve) transfer of each polytope SFP@C, OS@C, RP@C, PC@C, and CC@C half-cell cathode electrodes (R_{ct}) is related to the diameter of semicircular curvatures on the real Z [18,49, 50]. The actively reactive electrode surfaces are represented by the small diameter of its semicircular curvatures, indicating the low R_{ct} value. Among all half-scale cathode LIB-CR2032 coin-cells, the SFP@C half-cell cathode showed a lower R_{ct} value compared with all mesopolytope cathodes. This finding indicates that the sixteen-faceted exposure polyhedron (SFP@C) cathode exhibits rapid electrons/Li+ ions diffusion kinetics. Figure S11d shows evidence of the long-term cycle stability of the electrons/Li^+ ions movements along all polytope SFP@C, OS@C, RP@C, PC@C, and CC@C half-cell cathode electrode surfaces, as evidenced from the slight increase of R_{ct} values with 200th cycles. Significantly, due to the stability of the electron/Li^+-ion diffusivity and transportation kinetics of 3D SFP@C cathode polytope, this electrode attains lowest R_{ct} value among all OS@C, RP@C, PC@C, and CC@C half-cell cathode electrodes within 200th cycles. This finding indicates that the 3D SFP@C cathode electrode maintains its remarkable features in terms of (i) distribution of highly dense exposure active surface sites along multiple polygon tetragonal and triangular facet components, and (ii) high flexibility and mobility sites along edges, vertices, and terraces, and (iii) rapid transport and movement of electrons/Li^+ ions along axial, and frontal crystal planes during lithiation/delithiation processes.

Furthermore, the sustainable ~5 nm C-shell dot-dressers the outer surface layers of cathodes assist the structural electrode stability of mesopolytope geometrics during the high-temperature treatments. The retention geometrics and its topographic surfaces and multi-facet crystals improve the sustainability of electronic conductivity and transportation kinetics to withstand against high-temperature treatments (i.e., ~250–455 K) [51]. To check the thermal stability of all polytope SFP@C, OS@C, RP@C, PC@C, and CC@C half-cell cathode electrodes within temperature, we study the temperature dependence functionality vs the electrical conductivity for mesopolytope half-cell cathodes (Fig. S11c). Each polytope cathode electrode sustains its electronic conductivity and surface mobility at a wide range of temperature treatments. Among all polytope electrodes, the 16-

faceted SFP@C cathode shows high dynamic sustainability of atomic-scale crystallization along polygon facet components and then excellent conductivity at all exposed temperature ranges (~250–455 K).

Overall, the SFP@C electrode modulated in half-cell LIBs exhibit high Li$^+$ ion specific capacity, excellent rate reversibility and capability performance, and long-term cycle stability, and sustainability of electronic conductivity against highly-treated heating. These excellent electrochemical performances of the SFP@C half-cell cathode electrode are attributed to its polytope-key factors, as follows:

I. The vicinity formation of topographic surfaces such as meso-grooves, hole-mouth caves, and hollowness-like geodes in its mesopolytope crystal cores, thereby improving efficacy in Li insertion/extraction reaction for an 3D-LFPO@C electrode;
II. The well-ordered single-crystal-structures and orientations along 16-exposed active surface sites, thereby leading to the creation of high indices of truncated tetragonal and triangular facets, edges, vertices, and terraces for the open and wide potential ranges and high specific LIB-cathode capacities;
III. The heterogeneous high-index, and homeomorphic facets along axial, and frontal crystal planes enabled the mounting of 3D multi-diffusive directional gates for high gravimetric cell energy (Wh/kg), see supporting information S14.
IV. Defects along kinks, vertices, and ridges along the exterior SFP@ cathode surfaces might lead to facile electron/Li$^+$-ion movement during lithiation/delithiation processes;
V. The well-and large-coverage surface dispersion of thin nano-C dot shells along polygon SFP@C cathode layers plays an important role in preventing Fe dissolution or atomic dislocation (i.e.,

well-structured robustness) against severe treatment conditions, thereby enabling excellent sustainability of the electronic surface mobility and conductivity.

Half-scale 1D-TO@C capsule anode LIB-CR2032 coin-cells

The effectiveness of 1D-TO@C capsule geometrics as a potential anode electrode in the formulation of long-period cycle stability of half-scale anode LIB-CR2032 coin-cells in terms of (i) charging/discharging capacity cycling, and (ii) the capability performance rate is shown in Figure S12. The typical CV cell stability of half-scale 1D-TO@C anode LIB-CR2032 coin-cells within a potential window range of 1.0 V – 3.0 V vs. Li/Li^+ at 0.1C mV/s of a sweeping rate is studied at various cycling numbers (i.e., 1st - 500th cycles), as shown in Figure S12(a). The CV curves show two reduction/oxidation peaks at potential of 1.64 V and 2.1 V, indicating the cathodic (reduction of Ti^{4+} to Ti^{3+}) and anodic (oxidation of Ti^{3+} to Ti^{4+}) sweeps, respectively. The symmetric and spiculated peak profiles at 1.64 V and 2.1 V can be attributed to the Li^+-insertion (lithiation) and Li^+-extraction (delithiation) of 1D-Li_xTiO_2@C capsules, respectively. The sequential lithiation/delithiation cycles indicate the excellent cycling performance and high reversibility of 1D-TO@C anode despite the multiple-examined 500 cycles.

The potential charging/discharging curves of the 1st cycle capacity are recorded at at C-rates of 0.2, 0.5, 1, 5, 10, and 20 C mVs^{-1} and at potential range of 1.0–3.0 V vs. Li/Li^+. According to the Galvanostatic charging/discharging patterns, each discharge profile is firstly specified with a rapid decrease in potential from OCV–3 V (open circuit voltage) to 1.7 V vs. Li (Figure S12b).. Second, a linear plateau step of discharge pattern is distinct at 1.7 V, which refers to the lithiation process. Third, the gradual decrease in potential from 1.7 V (plateau linear zone) to cut-off voltage of 1.0 V vs. Li, thereby indicating the large amount of lithiation into interfacial Li^+ ion storage accommodation along the interior open-end mouth hole channels and mesogroove vicinities of 1D-TO@C-anode capsule.

The 1st cycle potential charging profiles are firstly increased in specific capacity at potential range of 1 V- 1.85 V vs. Li/Li$^+$(Figure S12b). The increase in charging pattern is indicated the monotonic Li$^+$-extraction (delithiation) process. Second, the continuous Li$^+$-extraction (delithiation) regime at potential range of 1.85 V- 2.1 V vs. Li/Li$^+$. Third, the curvature regime up to 3.00 V indicates the facile delithiation from solid electrode surface to electrolyte solution.

The 1st cycle discharge specific capacity values (mAh/g) of half-scale capsule 1D-TO@C anode LIB-CR2032 coin-cells at various C-rates (mV/s) in the range of 0.2C- 20C/ mVs^{-1} and at potential region of 1.0–3.0 V vs. Li/Li$^+$ (Figure S12c). The 1st discharge capacity values of half-scale capsule 1D-TO@C anode is decreased from 276.9 to 127.4 mAh/g by increasing the scan rates from 0.2 to 20C (mV/s). Figure S12d shows the Nyquist plot of half-scale capsule 1D-TO@C anode LIB-CR2032 coin-cells. This EIS result indicates the facile electron/Li$^+$-ion diffusivity and transportation kinetics along 1D-TO@C anode capsules.

The influence of structural stability of 1D-TO@C capsule geometrics in the rate capability performance of half-scale anode LIB-CR2032 coin-cells is shown in Figure S12e. The cycling discharge capacity performance (1st-100th range of cycle numbers) of 1D-TO@C capsule anode electrode at a potential region of 2–4.3 V vs. Li/Li$^+$ at C-rate range of 0.1C-20C (mV/s). The rate capability performance of half-scale 1D-TO@C capsule anode LIB-CR2032 coin-cells can be control under the following patterns: the discharge capacities at C-rates of 0.1C-5.0C are back to 0.1C and 10 C, and then followed by returning back to 1.0C and 20 C at 25 ^{o}C. We also preform the discharge capacity pattern of half-scale 1D-TO@C capsule anode LIB-CR2032 coin-cells at each C-rate (mV/s) within 10th cycles until reaching to 100th cycles. This rate capability profile of half-scale 1D-TO@C capsule anode indicates that first; the specific capacity (mAh/g) performance is decreased with the increase in C-rates (mV/s). Second, half-scale 1D-TO@C capsule anode shows excellent dischargeable and reversible capacity, approximately of 115.7 mAh g^{-1} at a 20 C sweep rate and after 100^{th} cycles during reversible Li^+-inclusion/-exclusion cycling processes.

Superscalable polytope SFP@C // capsule 1D-TO@C CR2032-coin cells and pouch LIB models

The key design of full-scale CR2032-coin LIB cells is based on mesopolytope SFP@C cathode with sustainable 1D-TO@C nanorod-like capsules (anode). The superscalable cathode/anode electrodes may offer multiple mass transports of electrons/Li^+ ions along their configuration and manipulation of formulated complex shapes, 1D and 3D directional gates (Figures 6, S1 and Scheme 1). In particular, the 3D SFP@C cathode polytopes also offer multiple polygon facet components along edges/vertices/ terraces, actively-reactive heterogeneous surface mobility sites, multi-grooves/caves, and coverage surface exposures.

In this full-scale CR2032-coin LIB cells, the reliable design is based on the excellent trade-off factors, in which a set of LIB-manufacture can be achieved with betterment safety without loss of the high energy density. The rational design of optimal tradeoff polytope SEP@C (P-electrode) and capsule 1D-TO@C (N-electrode) LIB model is mainly based on the mass ratios (.i.e., the balancing $(P/N)_{Cap}$ ratio ≈1.0: 1.07-1.1) that loaded 10 μm-Al-foils and 8 μm-Cu-foils. The key design configuration is achieved at specific $(P:N)_{Cap}$ ratio ≈1.0: 1.09, see supporting information S13.

Fig. 6

The specific discharging capacity ($mAhg^{-1}$) of full-scale mesopolytope SFP@C // capsule 1D-TO@C CR2032-coin cells is determined as a function of current C-rates at 0.1, 0.2, 0.5, 1, 2, 5, 10, and 20 C and at potential range of 0.9-3.5 V (Figure 6[A]). The discharge capacity profiles show excellent behavior along all C-rate ranges. The specific discharging capacity ($mAhg^{-1}$) is decreased with increasing C-rates, and attains a value of 132 mAhg^{-1} at 20 C. Our mesopolytope SFP@C cathode electrode is provided an excellent specific energy density of 426.9 Wh kg^{-1}. This value is effectively influenced by the specific key quantity-based mass fraction of P-electrode. For example, the mass% of SFP@C-material-based P-electrode cathode in full-scale LIB-CR2032-coin cells is approximately 43.8 % of the whole mass used for LIB components (see supporting information S13-S15). According to this mass fraction of cathode, the specific energy density of full-scale mesopolytope SFP@C // capsule 1D-TO@C LIB-CR2032-coin cell model is 186.98, and 177.81 186.98 Wh kg^{-1} at 0.1 C, and 1C, respectively (see supporting information S13). The high energy-density is a mandatory of long-driving range EVs.

The rate capability performance of full-scale mesopolytope SFP@C // capsule 1D-TO@C CR2032-coin cell design is evident, as shown in Figures 6(B) and (C). The rate capability profile is recorded along a wide potential range of 0.9–3.5 V and at various C-rate values of 0.1, 0.2, 0.5, 1, 2, and 5 C. The discharge profile of full-scale mesopolytope SFP@C // capsule 1D-TO@C CR2032-coin cell at C-rate range of 0.1C-5.0C is returned back to 0.1 and 10 C, and then followed by returning back to 1 and 20 C at 25 ^{o}C. At each C-rate (mV/s), the rate discharging capacities (mAhg^{-1}) are recorded with 10 cycles up to 100 cycles. Generally, the specific capacity of full-scale mesopolytope SFP@C // capsule 1D-TO@C LIB-CR2032-coin cell design decreases with increasing of C-rate values. The discharge cycling performance after 40 cycles (i.e., at 1 C-rate), and at 5 C-rate (i.e., after 60 cycles) is returned to 1 C-rate (after 90 cycles) and 20 C-rate (after 100 cycles), respectively. This discharge capacity at such specific C-rate profiles retains 99.6%, 99.2%, 98.7%, and 98.1% from the initial capacity of mesopolytope/capsule LIB-CR2032-coin cell design, respectively. The configuration hotkeys formulated with 1D and 3D directional transport gates, high-index components, active surface mobility sites, meso-grooved hollowness, and multifaceted mesopolytope exposure are controlled potential LIB-CR2032-coin cell design in terms of high specific energy density and outstanding rate capability (Scheme 1).

To fabricate pouch-type LIB models, ordered sets of multiple rolls of mesopolytope SFP@C // capsule 1D-TO@C LIB-CR2032-coin cells are packed-up in a collar fashion to form pouch LIB models (Scheme 1). A set of stacked layers of full-scale mesopolytope SEP@C cathode P-electrode // capsule 1D-TO@C anode N-electrode organized in pouch LIB-model is designated with specific 3D dimensions of 35 mm (width), 55 mm (length) and ~2.5-3mm (thickness), respectively. Well-packed and dense layers of 1D-TO@C-anode (5-layers/12-sides)//SFP@C-cathode (6-layers/12-sides) oriented in the coin cells are contiguously connected into a series of the built-in stacking layer configurations of pouch LIB-types, see supporting information S13, S14.

In order to optimize the full-cell mesopolytope SEP@C cathode P-electrode // capsule 1D-TO@C anode N-electrode LIBs, the total area of the cathode and anode coverage the pouch LIB cells are 150 and 143 cm^2; respectively. Therefore, the mass stacking of mesopolytope SEP@C cathode P-electrode and capsule 1D-TO@C anode N-electrode is 13.14 and 6.63 mg/cm^2, respectively. This finding indicates that the areal discharge capacity of the stacking mesopolytope SEP@C cathode P-electrode and capsule 1D-TO@C anode N-electrode is 1.144 and 1.145 Ah/cm^2, respectively (see supporting information S14). For practical/large-scale usage, the volumetric energy density of overall full-scale mesopolytope SEP@C cathode P-electrode // capsule 1D-TO@C anode N-electrode organized in LIB-model scales is controlling the preferable key shape-designed fashion of pouch models. Our experimental calculation shows that the volumetric energy density of pouch LIB-model is 242.83 Wh/L.

Fig. 7

Figure 7A shows cycling performance profiles of mesopolytope SFP@C // capsule 1D-TO@C LIB-CR2032-coin cell design in terms of charge/discharge capacity, and Coulombic performance efficacy. The cycling profiles (i.e., 1-2000 cycles) are carried out at 1 C-rate in a potential region from 0.9–3.5 V vs. Li/Li^+ at 25 °C. The cycling performance profiles of the first 200 cycles can be observed in Figure 7(B). Our mesopolytope SFP@C // capsule 1D-TO@C LIB-CR2032-coin cell design sets attain 93.4% from the first discharge capacity of 157.2 $mAhg^{-1}$ at 1C, even after 2000 cycles. Long term-stability in the Coulombic performance efficacy of ~99.89% is achieved at a rate of 0.1 C at 25 °C.

In such mesopolytope SFP@C // capsule 1D-TO@C LIB-CR2032-coin cell design systems, the superior electrochemical performance indicate the effectiveness of the buildup P-, N-electrodes with multiple mass transports along the 1D and 3D open-end directional gates, and multi-diffused channels and holes to potential occupant diffusions of Li^+ ions during the lithiation/delithiation (discharging/charging) cycling process. A high cycle number of full cell LIB-CR2032-coin cell design systems demonstrate ~100% of its Coulombic performance efficacy [50-53]. Scheme 1 shows evidence of the long-term structural stability of P- and N-electrode architectures, investigated by using FE-SEM, and elemental mapping analysis images (EDS), See Figure S14. The stability of sustainable anode//cathode architectures renders the robust formation of LIB designs after charge-discharge cycles (see supporting information S15). Thus, the outstanding stability of excellent electrochemical performance after 2000 cycles, the ~100% of Coulombic performance efficacy, high capacity at high rate capability, and long cycle life may be due to the excellent electronic contact, electrical conductivity, and facile transport along sustainable SFP@C//TO@C surfaces, compared with other reported LIB-designs using $LiFePO_4$//TiO_2 (cathode/anode) electrodes (See supporting information S16).

Conclusions

We design a powerful, full-scale LIB-CR2032-coin cell model that enables long-term storage cycles, continuous rate capability and charging/discharging stability, and excellent energy density. The superscalable half-, full-, and large-modulated LIB-models are fabricated by using heterogeneous mesopolytope 3D-LFPO@C cathode and capsule 1D-TO@C anode geometrics. In this LIB model system, multi-functional 3D-LFPO@C polytopes such as SFP@C, OS@C, RP@C, PC@C, and CC@C cathodes enabled fabrication of variable LIB model geometrics. We also study the hotkeys of mesopolytope 3D-LFPO@C cathode /capsule 1D-TO@C anode geometrics that feature 1D and 3D directional transport gates, high-index facets, active surface mobility sites, and hollowness and meso-grooves in potential full-scale LIBs. Among all remarkable 3D-LFPO@C cathode polytopes, the hybrid SFP@C hierarchy is a favored candidate for new-generation LIBs with excellent electrochemical performances. The superscalable polytope SFP@C// capsule 1D-TO@C LIB-CR2032-coin cell models are attained Coulombic performance efficacy of ~99.89%, discharge capacity of 93.4% after 2000 cycles, and high specific energy density ≈ 186.98 Wh.kg^{-1}, which overrides the requirement for long-driving range of EVs. Aside from the successful design of full-scale LIB-CR2032-coin cell, our intensive studies offer a control of a large scale pouch LIB models. In this pouch model, the P-, N- electrode LIB-CR2032-coin cell packing is designed in a collar fashion. Our finding indicates that the pouch-type LIBs offered high areal discharge capacities and remarkable gravimetric and volumetric energy and tap densities with high safety concerns, thereby configuring the scale-up requirements for next generation of EVs.

Associated Content

Supporting Information: Electrochemistry details, XRD pattern, FE-SEM and HR-TEM, nitrogen adsorption and desorption isotherms, Energy-dispersive X-ray spectroscopy (EDS), Thermal Analysis TG and DTA, FT-IR spectra, Raman spectra, X-ray photoelectron spectroscopy (XPS) analysis are provided. Electrochemical results of half-scale 1D-TO@C capsule anode LIB-CR2032 coin-cells (cyclic voltammetry at various sweep rates and cycle number, charge/discharge curves at various cycle numbers, Electrochemical impedance spectroscopy (EIS) and C-rate effect on discharge capacity) were supplied. Furthermore, key parameters of stacking layers of pouch-type LIB models such as (i) P-, and N-electrode cell capacity balancing, (ii) specific energy density, (iii) areal discharge capacity of cell battery, (iv) volumetric energy density and (v) stability of the mesopolytope cathode geometrics after multiple cycles are also supplied.

References

1- a) J. Liu, Addressing the Grand Challenges in Energy Storage, Adv. Funct. Mater., 23(8) (2013) pp.924-928, https://doi.org/10.1002/adfm.201203058; b) W. Luo, J.J. Gaumet, P. Magri, S. Diliberto, F. Li, P. Franchetti, J. Ghanbaja, L. Mai, Fast, green microwave-assisted synthesis of single crystalline Sb_2Se_3 nanowires towards promising lithium storage, J. Energy Chem., 30 (2019) pp. 27-33, https://doi.org/10.1016/j.jechem.2018.03.013; c) Z. Liu, Q. Yu, Y. Zhao, R. He, M. Xu, S. Feng, S. Li, L. Zhou, L. Mai., Chem. Soc. Rev., 48(2019) pp. 285-309. DOI: 10.1039/C8CS00441B

2- a) H. Gomaa M.A. Shenashen, H. Yamaguchi, A.S. Alamoudi, S.A. El-Safty, Extraction and recovery of Co^{2+} ions from spent lithium-ion batteries using hierarchal mesosponge γ-Al_2O_3 monolith extractors, *Green Chem.* **20** (2018), pp. 1841-1857, DOI10.1039/C7GC03673F ; b) H Gomaa, S. A. El-Safty, M. A. Shenashen, S. Kawada, H. Yamaguchi, M Abdelmottaleb, M. F. Cheira, Three-dimensional, Vertical Platelets of ZnO Carriers for Selective Extraction of Cobalt Ions from Waste Printed Circuit Boards, *ACS Sustain. Chem. Eng.* **6 (11)** (2018) pp. 13813-13825, https://pubs.acs.org/doi/abs/10.1021/acssuschemeng.8b01906; c) S. A. El-Safty, Md. R. Awual, M. A. Shenashen, A. Shahat, Simultaneous optical detection and extraction of cobalt(II) from lithium ion batteries using nanocollector monoliths, *Sens. Actuat. B* **176** (2013) pp. 1015– 1025, http://dx.doi.org/10.1016/j.snb.2012.09.040.

3- a) S. Li, Q. Wu, D. Zhang, Z. Liu, Y. He, Z.L. Wang, C. Sun, Effects of pulse charging on the performances of lithium-ion batteries, Nano Energy 56 (2019) p. 555–562, https://doi.org/10.1016/j.nanoen.2018.11.070; b) S. Nishimura, G. Kobayashi, K. Ohoyama, R. Kanno, M. Yashima, A. Yamada, Experimental visualization of lithium diffusion in Li_xFePO_4, Nat. Mater. 7 (2008) pp.707–711, doi:10.1038/nmat2251.

4- a) L. Guo, Y. Zhang, J. Wang, L. Ma, S. Ma, Y. Zhang, E. Wang, Y. Bi, D. Wang, W. C. McKee, Y. Xu, J. Chen, Q. Zhang, C. Nan, L. Gu, P. G. Bruc, Z. Peng, Unlocking the energy capabilities of micron-sized $LiFePO_4$, Nat. Commun. 6 (2015) p. 7898, doi: 10.1038/ncomms8898 (2015); b) Khalifa, H. et al. Sci. Reports 9 (2019) 14701; c) S. A. El-Safty, A. Reda, M. A. Shenashen, M. M. Selim, A. Elmarakbi H. A. Metawa, Theoretical and Experimental Sets of Choice Anode/Cathode Architectonics for High-Performance Full-Scale LIB Built-up Models, Nano-Micro Lett. 11 (2019), p. 84 https://doi.org/10.1038/s41598-019-51345-z.

5- a) W. Zhang, Y. Fu, W. Liu, L. Lim, X. Wang, A. Yu, A general approach for fabricating 3D MFe_2O_4 (M=Mn, Ni, Cu, Co)/graphitic carbon nitride covalently functionalized nitrogen-doped graphene nanocomposites as advanced anodes for lithium-ion batteries, Nano Energy 57 (2019) pp. 48–56, https://doi.org/10.1016/j.nanoen.2018.12.005; b) Y. Wang, P. He, H. Zhou, Olivine $LiFePO_4$: development and future, Energy Environ. Sci. 4 (2011) p. 805–817, DOI:10.1039/C0EE00176G.

6- Y. Jin, X. Tang, Y. Wang, W. Dang, J. Huang, X. Fang, High-tap density $LiFePO_4$ microsphere developed by combined computational and experimental approachesCrystEngComm, 20 (2018) p. 6695–6703, DOI: 10.1039/c8ce00894a.

7- M. Zhang, N. Garcia-Araez and A. L. Hector, Understanding and development of olivine $LiCoPO_4$ cathode materials for lithium-ion batteries, J. Mater. Chem. A, 6 (2018) p. 14483–14517, DOI:10.1039/C8TA04063J.

8- Y. Jiang, R. Tian, H. Liu, J. Chen, X. Tan, L. Zhang, G. Liu, H. Wang, L. Sun, W. Chu, Synthesis and characterization of oriented linked $LiFePO_4$ nanoparticles with fast electron and ion transport for high-power lithium-ion batteries, Nano Res., 8 (2015) p. 3803–3814, https://doi.org/10.1007/s12274-015-0879-7.

9- A.V. Murugan, T. Muraliganth, A. Manthiram. Rapid, Facile Microwave-Solvothermal Synthesis of Graphene Nanosheets and Their Polyaniline Nanocomposites for Energy Strorage, Chem. Mater. 21 (2009) p. 5004–5006, https://doi.org/10.1021/cm902413c.

10- N. Nitta, F. Wu, J. T. Lee, G. Yushin, Li-ion battery materials: present and future, Materialstoday 18(5) (2015) p. 252-264, https://doi.org/10.1016/j.mattod.2014.10.040; b) Y. Liu, et al., Nat. Commun. 9 (2018) pp. 1–8; (c) M.Y. Emran M. A. Shenashen, M. Mekawy, A.M. Azzam, N. Akhtar, H. Gomaa, M.M. Selim, A. Faheem, S.A. El-Safty, Ultrasensitive in-vitro monitoring of monoamine neurotransmitters from dopaminergic cells, Sens. Actuators B 259 (2018) pp. 114-124, https://doi.org/10.1016/j.snb.2017.11.156.

11- a) M.Y. Emran, M. Mekawy, N. Akhtar, M. A. Shenashen, I.M. El-Sewify. A. Faheem, S.A. El-Safty, Broccoli-shaped biosensor hierarchy for electrochemical screening of noradrenaline in living cells, Biosens. Bioelectron. 100 (2018) p. 122-131, https://doi.org/10.1016/j.bios.2017.08.050; b) MY Emran, S. A. El-Safty, M. A Shenashen, T Minowa, A well-thought-out sensory protocol for screening of oxygen reactive species released from cancer cells, Sens. Actuat. B 284(2019) p. 456-467, https://doi.org/10.1016/j.snb.2018.12.142; c) M. Y. Emran, M. A. Shenashen, H. Morita, S. A. El-Safty, 3D-Ridge Stocked Layers of Nitrogen-Doped Mesoporous Carbon Nanosheets for Ultrasensitive Monitoring of Dopamine Released from PC12 Cells under K^+ Stimulation, Adv. Healthcare Mater. 7 (16) (2018) p. 1701459, https://doi.org/10.1002/adhm.201701459; d) M. Y. Emran, M. A. Shenashen, A. A. Abdelwahab, H. Khalifa, M. Mekawy, N. Akhtar M. Abdelmottaleb, S.A. El-Safty, "Design of hierarchical electrocatalytic mediator for one step, selective screening of biomolecules in biological fluid samples, J. Appl. Electrochem. 48(5) (2018) p. 529–542, https://doi.org/10.1007/s10800-018-1175-5.

12- a) S.-Y. Chung, J.T. Bloking, Y.-M. Chiang, Electronically conductive phospho-olivines as lithium storage electrodes. Nat. Mater. 1(2) (2002) p. 123–128, doi:10.1038/nmat732; b) H. Khalifa, S. A. El-Safty, A. Reda, M. A. Shenashen, A. Elmarakbi H. A. Metawa, Structurally folded curvature surface models of geodes/ agate rosettes (cathode/anode) as vehicle/truck storages for high energy density of LIBs, Batteries Supercaps (2019) doi.org/10.1002/batt.201900083

13- J. Liu, J. Wang, X. Yan, X. Zhang, G. Yang, A.F. Jalbout, R. Wang, Long-term cyclability of $LiFePO_4$/carbon composite cathode material for lithium-ion battery applications, Electrochim. Acta, 54(2009) p. 5656–5659, https://doi.org/10.1016/j.electacta.2009.05.003.

14- G. Liang, L. Wang, X. Ou, X. Zhao and S. Xu, Lithium iron phosphate with high-rate capability synthesized through hydrothermal reaction in glucose solution, J. Power Sources, 184(2008) pp. 538–542, https://doi.org/10.1016/j.jpowsour.2008.02.056.

15- M. Wagemaker, B.L. Ellis, D. Lützenkirchen-Hecht, F.M. Mulder, L.F. Nazar. Proof of Supervalent Doping in Olivine $LiFePO_4$, Chem. Mater. 20 (2008) p. 6313–6315, https://doi.org/10.1021/cm801781k.

16- H. Liu, H. Yang, J. Li. A novel method for preparing $LiFePO_4$ nanorods as a cathode material for lithium-ion power batteries, Electrochim. Acta 55 (2010) p. 1626–1629, https://doi.org/10.1016/j.electacta.2009.10.039.

17- I. Belharouak, C. Johnson, K. Amine. Synthesis and electrochemical analysis of vapor-deposited carbon-coated $LiFePO_4$, Electrochem. Commun. 7 (2005) p. 983–988, https://doi.org/10.1016/j.elecom.2005.06.019.

18- G. Qin, S. Xue, Q. Ma, C. Wang, The morphology controlled synthesis of 3D networking $LiFePO_4$ with multiwalled-carbon nanotubes for Li-ion batteries, CrystEngComm, 16 (2014) p. 260–269, DOI:10.1039/C3CE41967C.

19- a) N. Akhtar, S. A. El-Safty, M. Khairy, W. Ahmed, Chemosensors 2(4), (2014) p. 235-250; c) N. Akhtar, S. A. El-Safty, M Khairy, WA El-Said, Fabrication of a highly selective nonenzymatic amperometric sensor, for hydrogen peroxide based on nickel foam/cytochrome c modified electrode Sens. Actuat. B 207, (2015) p. 158-166, https://doi.org/10.1016/j.snb.2014.10.038.

20- a) Z. Tian, Z. Zhou, S. Liu, F. Ye, S. Yao. Enhanced properties of olivine $LiFePO_4$/graphene co-doped with Nb^{5+} and Ti^{4+} by a sol–gel method, Solid State Ionics 278 (2015) p. 186–191, https://doi.org/10.1016/j.ssi.2015.06.017; b) X. Qin, J. Wang, J. Xie, F. Li, L. Wen, X. Wang. Hydrothermally synthesized $LiFePO_4$ crystals with enhanced electrochemical properties: simultaneous suppression of crystal growth along [010] and antisite defect formation, Phys. Chem. Chem. Phys. 14 (2012) p. 2669–2677, DOI:10.1039/C2CP23433E.

21- M.K. Devaraju, I. Honma. Hydrothermal and Solvothermal Process Towards Development of $LiMPO_4$ (M = Fe, Mn) Nanomaterials for Lithium-Ion Batteries, Adv. Energy Mater. 2 (2012) p. 284–297, https://doi.org/10.1002/aenm.201100642.

22- A. Singhal, G. Skandan, G. Amatucci, F. Badway, N. Ye, A. Manthiram, H. Ye, J.J. Xu. Nanostructured electrodes for next generation rechargeable electrochemical devices, J. Power Sources 129 (2004) p. 38–44, https://doi.org/10.1016/j.jpowsour.2003.11.010.

23- K.S. Park, J. T. Son, H. T. Chung, S. J. Kim, C. H. Lee, K. T. Kang and H. G. Kim, Surface modification by silver coating for improving electrochemical properties of $LiFePO_4$, Solid State Commun. 129 (2004) p. 311–314.

24- M. Takahashi, S. Tobishima, K. Takei, Y. Sakurai. Characterization of $LiFePO_4$ as the cathode material for rechargeable lithium batteries, J. Power Sources 97–98 (2001) p. 508–511, https://doi.org/10.1016/S0378-7753(01)00728-5.

25- T.H. Cho, H.T. Chung. Synthesis of olivine-type $LiFePO_4$ by emulsion-drying method, J. Power Sources 133 (2004) p. 272–276, https://doi.org/10.1016/j.jpowsour.2004.02.015.

26- S. Lee, Y. Cho, H. K. Song, K. T. Lee and J. Cho, Carbon-coated single-crystal $LiMn_2O_4$ nanoparticle clusters as cathode material for high-energy and high-power lithium-ion batteries, Angew. Chemie - Int. Ed., 51(2012) p. 8748–8752, doi: 10.1002/anie.201203581.

27- M. Wang, Y. Yang, Y. Zhang. Synthesis of micro-nano hierarchical structured $LiFePO_4$/C composite with both superior high-rate performance and high tap density Nanoscale 3 (2011) p. 4434–4439, DOI:10.1039/C1NR10950B.

28- a) B. Guo, H. Ruan, C. Zheng, H. Fei and M. Wei, Hierarchical $LiFePO_4$ with a controllable growth of the (010) facet for lithium-ion batteries, Sci. Rep. 3(2013) p. 2788, https://doi.org/10.1038/srep02788; b)K. Dokko, S. Koizumi, H. Nakano and K. Kanamura. Particle morphology, crystal orientation, and electrochemical reactivity of $LiFePO_4$ synthesized by the hydrothermal method at 443 K, J. Mater. Chem., 17(2007) p.4803–481, DOI:10.1039/B711521K.

29- a) M. A. Shenashen, D. Hassen, S. A. El-Safty, H.Isago, A. Elmarakbi, H. Yamaguchi, Axially oriented tubercle vein and X-crossed sheet of N-Co_3O_4@C hierarchical mesoarchitectures as potential heterogeneous catalysts for methanol oxidation reaction, Chem. Eng. J. 313(2017) p. 83–98, https://doi.org/10.1016/j.cej.2016.12.003; b) D. K. Hassen, M.M. Selim, S. A. El-Safty, K. A. Khalil, G. Abu el-Maged, M. Dewidar, Nano-Structures & Nano-Objects 9 (2017) p. 31-39; c) D. Hassen, S. A. El-Safty, K. D. Hassen, S. A. El-Safty, N. Akhtar, A. Chatterjee, A. Elmarakbi, Mesoscopic Fabric Sheet Racks and Blocks as Catalysts with Efficiently Exposed Surfaces for Alcohol Electrooxidation, Adv. Mater. Interfaces 3(24) (2016) p. 1600743, https://doi.org/10.1002/admi.201600743.

30- J.-M. Tarascon, P. Poizot, S. Laruelle, S. Grugeon and L. Dupont. Nature, 407(2000) p.496–499.

31- Y.S. Hu, L. Kienle, Y.G. Guo, J. Maier, High Lithium Electroactivity of Nanometer-Sized Rutile TiO_2, Adv. Mater. 18 (2006) p. 1421–1426, https://doi.org/10.1002/adma.200502723.

32- Y. Wang, M. Wu, W.F. Zhang. Preparation and electrochemical characterization of TiO_2 nanowires as an electrode material for lithium-ion batteries, Electrochim. Acta 53 (2008) p. 7863–7868, https://doi.org/10.1016/j.electacta.2008.05.068.

33- a) J. Wang, Y. Bai, M. Wu, J. Yin, W.F. Zhang. Preparation and electrochemical properties of TiO_2 hollow spheres as an anode material for lithium-ion batteries, J. Power Sources 191 (2009) p. 614–618, https://doi.org/10.1016/j.jpowsour.2009.02.056; b) G. Wang, et al., Energy Technol., (2018) pp. 1–29; c) M. S. Selim, S.A. El-Safty A. M. Azzam M. A. Shenashen M. A. El-Sockary O. M. Abo Elenien, Superhydrophobic Silicone/TiO_2–SiO_2 Nanorod-like Composites for Marine Fouling Release Coatings, ChemistrySelect, **4(12)** (2019) p. 3395-3407, https://doi.org/10.1002/slct.201803314.

34- a) M. Khairy, S. A. El-Safty, Hemoproteins-nickel foam hybrids as effective supercapacitors. Chem. Commun. 50(2014) pp. 1356-1358, https://doi.org/10.1039/c3cc48155g; b) M. Khairy, S. A. El-Safty, Promising supercapacitor electrodes based immobilization of proteins onto macroporous Ni foam materials, J. Energy Chem., 24 (1) (2015) pp. 31-38, https://doi.org/10.1016/S2095-4956(15)60281-9; c) H. Khalifa, S. A. El-Safty, M. A. Shenashen, A. Reda, A. Elmarakbi H. A. Metawa, , Large-Scale Giant Architectonic Electrodes Designated with Complex Geometrics and Super Topographic Surfaces for Fully Cycled Dynamic LIB Modules, Energy Storage Mater. (2019) doi.org/10.1016/j.ensm.2019.12.009; d) M. Khairy, S. A. El-Safty, Sens. Actuat. B, 193(2014) pp. 644-652; d) M. Khairy, S. A. El-Safty, RSC Adv., 3(2013) pp. 23801-23809.

35- D.-H. Lee, B.H. Lee, A.K. Sinha, J.H. Park, M.S. Kim, J. Park, H. Shin, K.S., Lee, Y.E. Sung, T. Hyeon, Engineering Titanium Dioxide Nanostructures for Enhanced Lithium-Ion Storage, J. Am. Chem. Soc., 140(2018) p.16676–16684, https://doi.org/10.1021/jacs.8b09487.

36- V. Aravindan, Y.S. Lee, R. Yazami, S. Madhavi. TiO_2 polymorphs in 'rocking-chair' Li-ion batteries, MaterialsToday 18 (2015) p. 345–351, https://doi.org/10.1016/j.mattod.2015.02.015; b) G.F. Ortiz, I. Hanzu, T. Djenizian, P. Lavela, J.L. Tirado, P. Knauth, Alternative Li-Ion Battery Electrode Based on Self-Organized Titania Nanotubes, Chem. Mater. 21 (2009) pp. 63–67, https://doi.org/10.1021/cm801670u.

37- a) W. Warkocki, S. A. El-Safty, M. A. Shenashen, E. Elshehy, H. Yamaguchi, N. Akhtar, optical detection, and separation of noxious SeO32− using a mesoporous nanotube hybrid membrane, J. Mater. Chem. A., 3(34) (2015) pp. 17578-17589, http://dx.doi.org/10.1039/C5TA02827B; b) H.G. Gomaa, H. Khalifa, M. Selim, M. A. Shenashen, S. Kawada, A.S. Alamoudi, A. Azzam, A. Alhamid, S.A. El-Safty, Selective, photo-enhanced trapping/detrapping of arsenate anions using mesoporous blobfish head TiO_2 monoliths, ACS Sustain. Chem. Eng., 5 (11) (2017) pp. 10826–10839, https://pubs.acs.org/doi/abs/10.1021/acssuschemeng.7b02766; c) A. Aboelmagd, S. A. El-Safty, M. A. Shenashen, E. A. Elshehy, M. Khairy, M. Sakaic, H. Yamaguchi, Nanomembrane Canister Architectures for Visualization and Filtration of Oxyanion Toxin in One-step Processing, Chem. Asian J., 10 (11) (2015) pp. 2467-2478, https://doi.org/10.1002/asia.201500565.

38- J. Sundaramurthy, V. Aravindan, P. S. Kumar, S. Madhavi, S. Ramakrishna. Electrospun $TiO_{2-\delta}$ Nanofibers as Insertion Anode for Li-Ion Battery Applications, J. Phys. Chem. C 118 (2014) p. 16776–16781, dx.doi.org/10.1021/jp412787z.

39- X. Zhang, V. Aravindan, P. S. Kumar, H. Liu, J. Sundaramurthy, S. Ramakrishna, S. Madhavi, Nanoscale 5 (2013) p. 5973–5980, DOI:10.1039/C3NR01128C.

40- G. Chen, X. Song, T.J. Richardson. Metastable Solid-Solution Phases in the $LiFePO_4/FePO_4$ System, J. Electrochem. Soc. 154 (2007) pp. A627-A632, DOI: 10.1149/1.2732189.

41- F. Wang, X. Wang, Z. Chang, Y. Zhu, L. Fu, X. Liu, Y. Wu. Electrode materials with tailored facets for electrochemical energy storage, Nanoscale Horizons 1 (2016) p. 272–289, DOI:10.1039/C5NH00116A.

42- C. Sun, S. Rajasekhara, J. B. Goodenough and F. Zhou, Monodisperse Porous $LiFePO_4$ Microspheres for a High Power Li-Ion Battery Cathode, J. Am. Chem. Soc., 133(2011) p. 2132–2135, https://doi.org/10.1021/ja1110464.

43- N. Akhtar, M.Y. Emran, M. A. Shenashen, H. Khalifa, T. Osaka, A. Faheem, T. Homma, H. Kawarada, S.A. El-Safty, Fabrication of Photo-electrochemical biosensor for ultrasensitive screening of mono-bioactive molecules: effect of geometrical structures and crystal surfaces J. Mater. Chem. B 5 (**2017**) p. 7985–7996, DOI: 10.1039/C7TB01803G.

44- a) I. M. El-Sewify, M. A. Shenashen, A. Shahat, H. Yamaguchi, M. M. Selim, M. M.H. Khali, S. A. El-Safty, Dual Colorimetric and Fluorometric Monitoring of Bi3+ Ions in Water using Supermicroporous Zr-MOFs Chemosensors J. Luminescence. **198** (2018) p. 438-448, https://doi.org/10.1016/j.jlumin.2018.02.028; b) I. M. El-Sewify, M. A. Shenashen, A. Shahat, M. M. Selim, M. M.H. Khalil, S.. A. El-Safty, Sensitive and selective fluorometric determination and monitoring of Zn^{2+} ions using supermicroporous Zr-MOFs chemosensors, Microchemical J., **139** (2018) p. 24-33, https://doi.org/10.1016/j.microc.2018.02.002; c) S. A. El-Safty, M.A. Shenashen, M. Ismael, M. Khairy, Mesocylindrical Aluminosilica Monolith Biocaptors for Size-Selective

Macromolecule Cargos, Adv. Funct. Mater. 22 (**2012**) p. 3013–3021, https://doi.org/10.1002/adfm.201200393.

45- D. Hassen, M. A. Shenashen, S. A. El-Safty, M.M. Selim, H. Isago, A. Elmarakbi, A. El-Safty, H. Yamaguchi, Nitrogen-doped carbon-embedded TiO2 nanofibers as promising oxygen reduction reaction electrocatalysts, J. Power Sources 330 (**2016**) p. 292-303, http://dx.doi.org/10.1016/j.jpowsour.2016.08.140.

46- H. Gomaa, M. A. Shenashen, H. Yamaguchi, A. S. Alamoudi, M. Abdelmottaleb, M. F. Cheira, T. A. Seaf El-Naser, S.A. El-Safty, Highly-efficient removal of AsV, Pb^{2+}, Fe^{3+}, and Al^{3+} pollutants from water using hierarchical, microscopic TiO_2 and $TiOF_2$ adsorbents through batch and fixed-bed columnar techniques, J. Cleaner Production, 182 (**2018**) p. 910-925, https://doi.org/10.1016/j.jclepro.2018.02.063.

47- M. A. Shenashen, S. Kawada, M. M. Selim, W. M. Morsy, H. Yamaguchi, A. A. Alhamid, N. Ohashi, I. Ichinose, S.A. El-Safty, Bushy Sphere Dendrite with Husk-shaped Branches Axially Spreading out from Its Core for Photo-catalytic Oxidation/ Remediation of Toxins Nanoscale 9 (**2017**) p. 7947-7959, http://dx.doi.org/10.1039/C7NR01092C, DOI: 10.1039/C7NR01092C; b) M. A. Shenashen, N. Akhtar, M. M. Selim, W. M. Morsy, H. Yamaguchi, S. Kawada, A. A. Alhamid, N. Ohashi, I. Ichinose, A.S. Alamoudi, S.A. El-Safty, Effective, Low-Cost Recovery of Toxic Arsenate Anions from Water by Using Hollow-Sphere Geode Traps, Chem. Asian J., 12(15) (**2017**) p. 1952–1964, https://doi.org/10.1002/asia.201700666.

48- J. Zhang, J. Lu, D. Bian, Z. Yang, Q. Wu and W. Zhang, Solvothermal Synthesis of Hierarchical $LiFePO_4$ Microplates with Exposed (010) Faces as Cathode Materials for Lithium Ion Batteries, Ind. Eng. Chem. Res., 53(2014) p. 12209–12215, https://doi.org/10.1021/ie501743b.

49- W. Zhang, X. Zhou, X. Tao, H. Huang, Y. Gan, C. Wang, In situ construction of carbon nano-interconnects between the $LiFePO_4$ grains using ultra low-cost asphalt, Electrochim. Acta 55 (2010) p. 2592–2596, https://doi.org/10.1016/j.electacta.2009.11.072.

50- a) M. A. Shenashen, D. Hassen, S. A. El-Safty, H.Isago, A. Elmarakbi, H. Yamaguchi, Axially oriented tubercle vein and X-crossed sheet of N-Co_3O_4@C hierarchical mesoarchitectures as potential heterogeneous catalysts for methanol oxidation reaction, Chem. Eng. J., 313 (2017) p. 83–98, https://doi.org/10.1016/j.cej.2016.12.003; b) M.Y. Emran, M.A. Shenashen, H. Morita, S. A. El-Safty, One-step selective screening of bioactive molecules in living cells using sulfur-doped microporous carbon Biosens. Bioelectron.190(30) (2018) p. 237-245; c) M. Y. Emran, et al., Electrocatalysis, 9(2018) p. 514–525; d) M.Y. Emran, M.A. Shenashen, A.A. Abdelwahab, M.

Abdelmottaleb, S. A. El-Safty, Facile synthesis of microporous sulfur-doped carbon spheres as electrodes for ultrasensitive detection of ascorbic acid in food and pharmaceutical products, New J. Chem. 42(2018) p. 5037-5044, DOI: 10.1039/C7NJ05047J.

51- a) N. Akhtar, S. A. El-Safty, M. E Abdelsalam, M. Shenashen, H. Kawarada, Radially oriented nanostrand electrodes to boost glucose sensing in mammalian blood, Biosens. Bioelectron. 77 (2016) p. 656–665, https://doi.org/10.1016/j.bios.2015.10.023; b) M.Y. Emran, H. Khalifa, H. Gomaa, M. A. Shenashen, N. Akhtar, M. Mekawy, A. Faheem, S. A. El-Safty, Hierarchical C-N doped NiO with dual-head echinop flowers for ultrasensitive monitoring of epinephrine in human blood serum, Microchimica Acta 184(2017) p. 4553–4562, https://doi.org/10.1007/s00604-017-2498-3; c) N. Akhtar, S. A. El-Safty, M. E Abdelsalam, H. Kawarada, Adv. Healthcare Mater. 4(14) (2015) p. 2110-2119; d) N. Akhtar, S. A. El-Safty, M. E Abdelsalam, H. Kawarada, Nano-Structures & Nano-Objects, 2(2015) p. 35-44.

52- D. Hassen, M. A. Shenashen, A. R. El-Safty, A. Elmarakbi, S. A. EL-Safty, Anisotropic N-Graphene-diffused Co3O4nanocrystals with dense upper-zone top-on-plane exposure facets as effective ORR electrocatalysts, Sci. Rep. 8 (2018) p. 3740, https://doi.org/10.1038/s41598-018-21878-w.

53- D. Hassen, S. A. El-Safty, K. Tsuchiya, A. Chatterjee, A. Elmarakbi, M. A. Shenashen, M Sakai, Longitudinal Hierarchy Co3O4 Mesocrystals with High-dense Exposure Facets and Anisotropic Interfaces for Direct-Ethanol Fuel Cells, Sci. Rep. 6 (2016) p. 24330, https://doi.org/10.1038/srep24330.

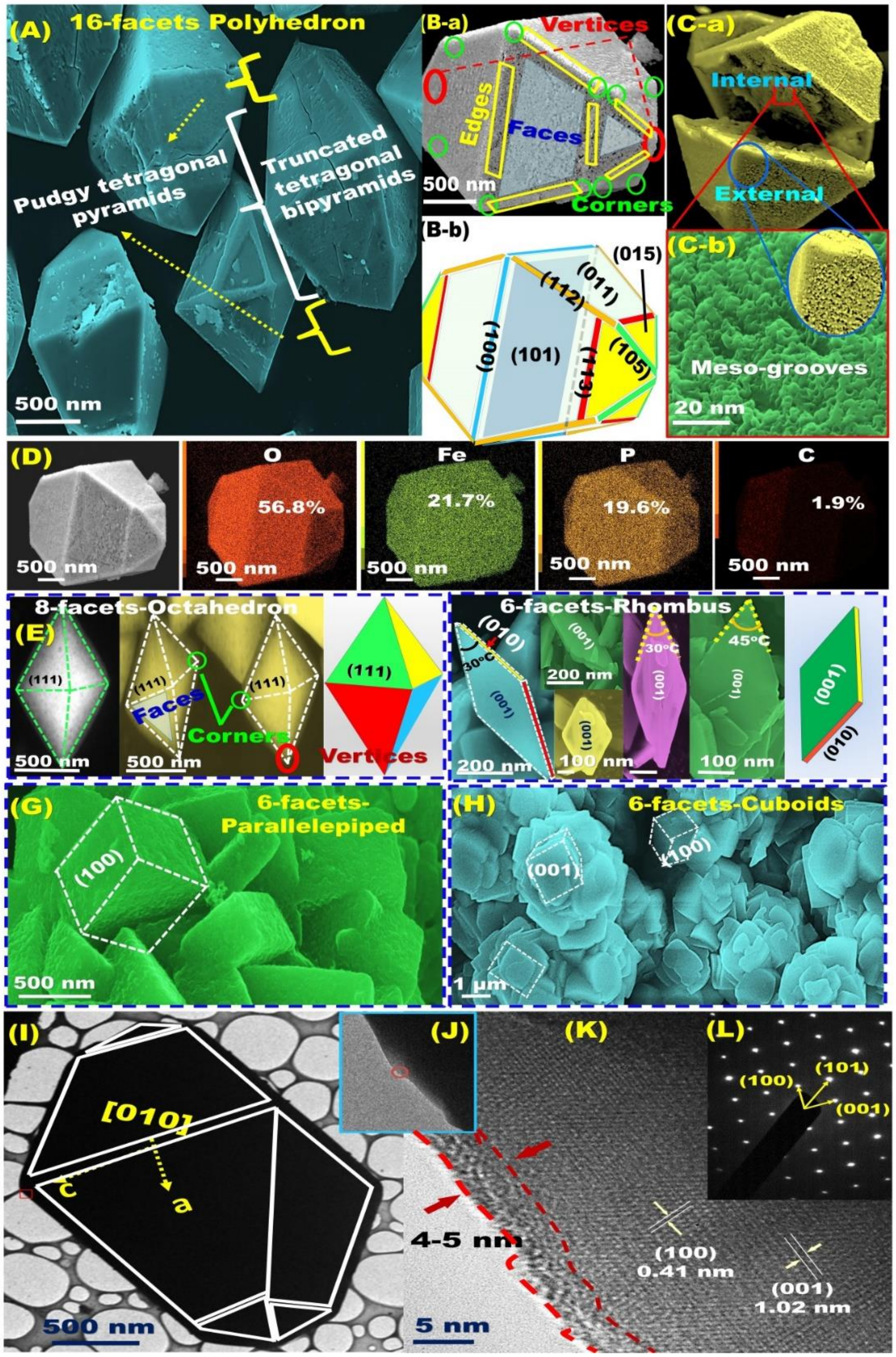

Fig. 1 (A-a) Low magnification FE-SEM and (B-a) high magnifications FE-SEM of heterogeneous high-index sixteen-faceted polyhedron architectures, labeled as (SFP@C), with active espoused facets. (C-a) 3D pattern of SFP polytope divided into two lobes at truncated splitting edge. Insets of (C-a) show with high magnification FE-SEM image of grooves inside hollowness-like geode caves at the core of SFP@C. (D) Energy-dispersive X-ray spectroscopy (EDX) and elemental mapping

analysis (mass ratios) of SFP@C mesopolytope of O (56.8%), Fe (21.7%0, P (19.6%), C (1.9%), respectively. (E), (F), (G) and (H) High magnification images and schematic drawing of mesopolytopes octahedron simplex (OS@C), rhombus platelet (RP@C), parallelepiped complex object (PC@C), and convex complex (CC@C) structures; respectively. (I) and (J) Low and high magnification HR-TEM micrographs of SFP@C cathode. (K) High magnification HR-TEM of polyhedron lattice pattern at edge with clear thin layer 4-5 nm of C-coating on surface of SFP crystals. (L) Selected area electron diffraction (SAED) pattern image of SFP@C unit block with incident beam along the [010] crystallographic direction indicating the formation of single crystal of orthorhombic LFPO olivine mesocrystals with the SFP@C unit blocks.

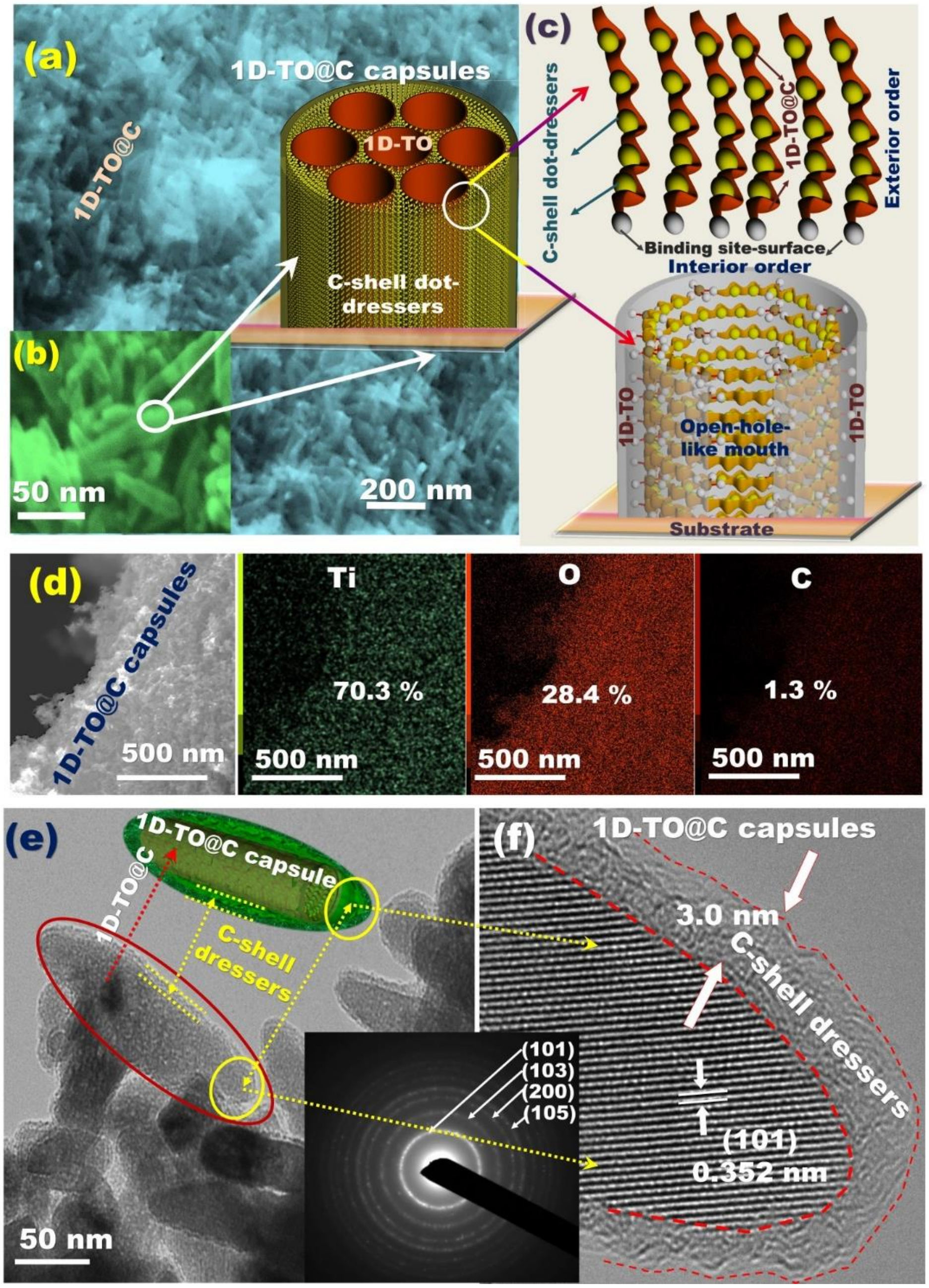

Fig. 2 (a & b) Low and high magnification FE-SEM and interior/exterior order organization of nano-C layers along the entire 1D-TO@C capsules. (c) 3D projects of open-end directional gate of 1D-TO@C capsules oriented in anodic electrode. (d) Energy-dispersive X-ray spectroscopy (EDX) and elemental mapping analysis of top-view surfaces of 1D-TO@C capsules. The elemental mapping of 1D-TO@C composite of well-dispersed C-shell like layers along NRs with percentage ratio 70.3:28.4:1.4% corresponding to O: Ti: C elements, respectively. (e) HR-TEM micrographs of 1D-TO@C capsules. (e-insert) Representative 1D objects of open-end nanorod capsules. (f) High magnification HR-TEM pattern at lattice-edge of 1D-TO capsules. The inset of pattern (f) of the corresponding electron diffraction (ED) pattern, and (e-inset) schematic illustration of anodic 1D-TO@C electrodes.

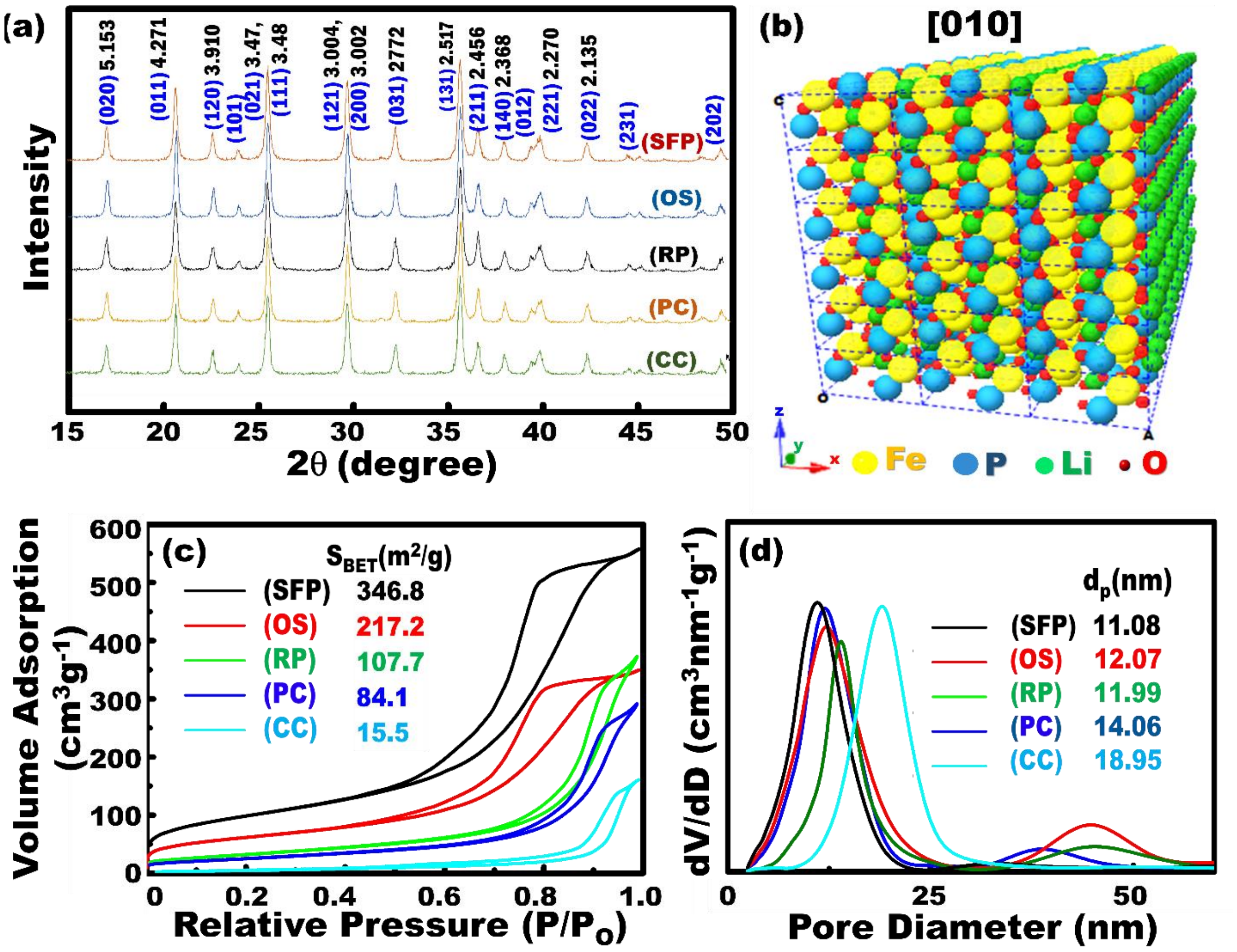

Fig.3 **(a)** XRD patterns of 3D-LiFePO4@C (3D-LFPO@C) mesopolytopes with different structures, facets and morphologies: sixteen-faceted exposure polyhedron (SFP@C), octahedron simplex (OS@C), rhombus platelet (RP@C), parallelepiped complex object (PC@C), and convex complex (CC@C) mesopolytopes. **(b)** Crystal structure of olivine-LFPO (16-faceted polyhedron architecture SFP material) at direction [010] plane. (c) Nitrogen adsorption-desorption isotherms, (inset-c) surface areas in m^2/g and **(d)** the corresponding pore-size distribution curves, including summary of pore diameter in nm calculated by nonlinear density functional theory (NLDFT) method from the adsorption branch for all 3D-LFPO@C mesopolytopes.

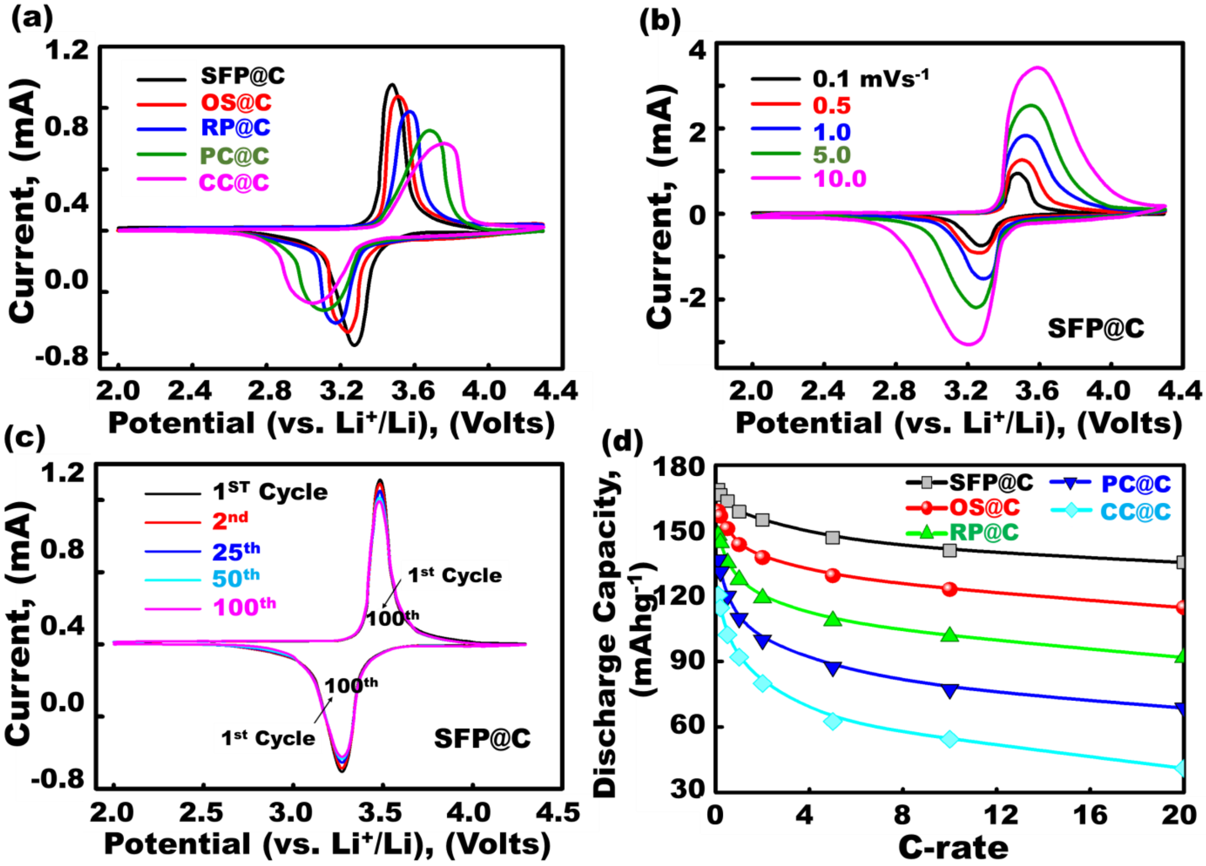

Fig. 4 (a, b and c) Cyclic voltammograms (CVs) and electrochemical performances of mesopolytope 3D-LFPO@C half-scale cathode LIB-CR2032 coin-cells. **(a)** CV curves of variable homeomorphic electrode surfaces such as SFP@C, OS@C, RP@C, PC@C, and CC@C mesopolytopes, respectively. **(b)** CV curves of SFP@C half-cell cathode at different sweep rates of 0.1, 0.5, 1, 5 and 10 mVs^{-1}. **(c)** CV curves of SFP@C half-cell cathode at different cycle numbers from 1-100 cycles at 0.1 mVs^{-1}. **(d)** First discharge capacity of 3D-LFPO@C mesopolytopes based on SFP@C, OS@C, RP@C, PC@C and CC@C, respectively at a current rate 0.1C -20C of cathode half-cell LIBs. All electrochemical measurements for mesopolytope half-cell 3D-LFPO@C cathodes were operated within voltage range of (2.0-4.3 V), at 25 ºC.

(A)

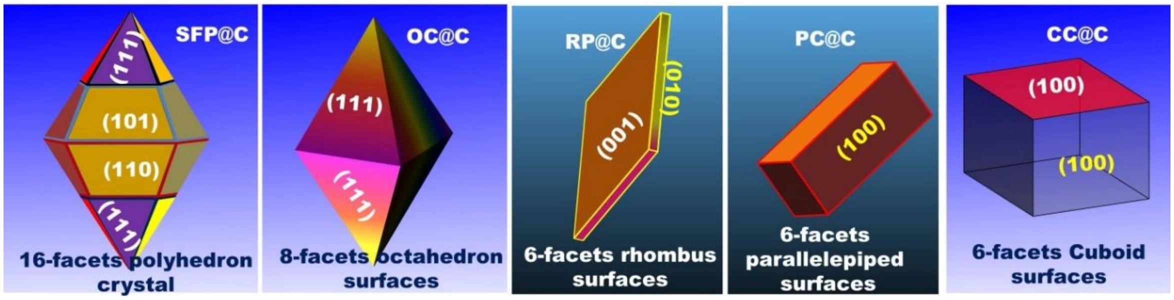

(B)

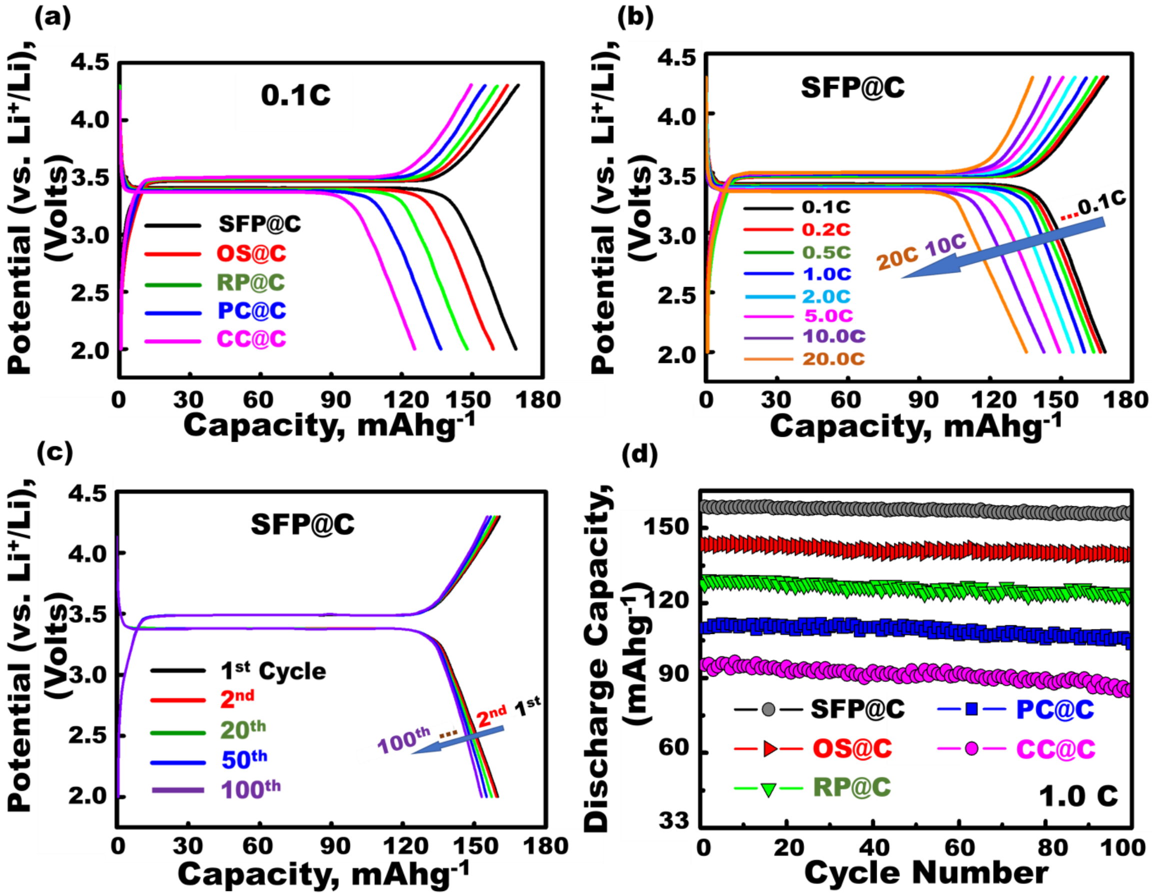

Fig. 5 (A) Design of 3D multifaceted geometrics of variable homeomorphic electrode surfaces such as SFP@C, OS@C, RP@C, PC@C, and CC@C mesopolytopes. (B,a-d) Effect of variable model geometrics and multifaceted exposure sites of mesopolytopes on the charge-discharge voltage profiles. (B-a) First cycle half-cell cathodes of 3D-LFPO@C mesopolytopes based on SFP@C, OS@C, RP@C, PC@C and CC@C, respectively at current rate 0.1C. **(B-b)** First cycle half-cell SFP@C cathode at different C-rates (i.e., 0.1C to 20C range). **(B-c)** The 16-faceted polyhedron structure SFP@C half-cell cathode at a current rate 1.0C and at different cycle number up to 100 cycles. (B-d) Cycling performance stability for variable cathode model geometrics SFP@C, OS@C, RP@C, PC@C and CC@C in half-scale cathode LIB-CR2032-coin cells, at rate of 0.1C for 100 cycles.

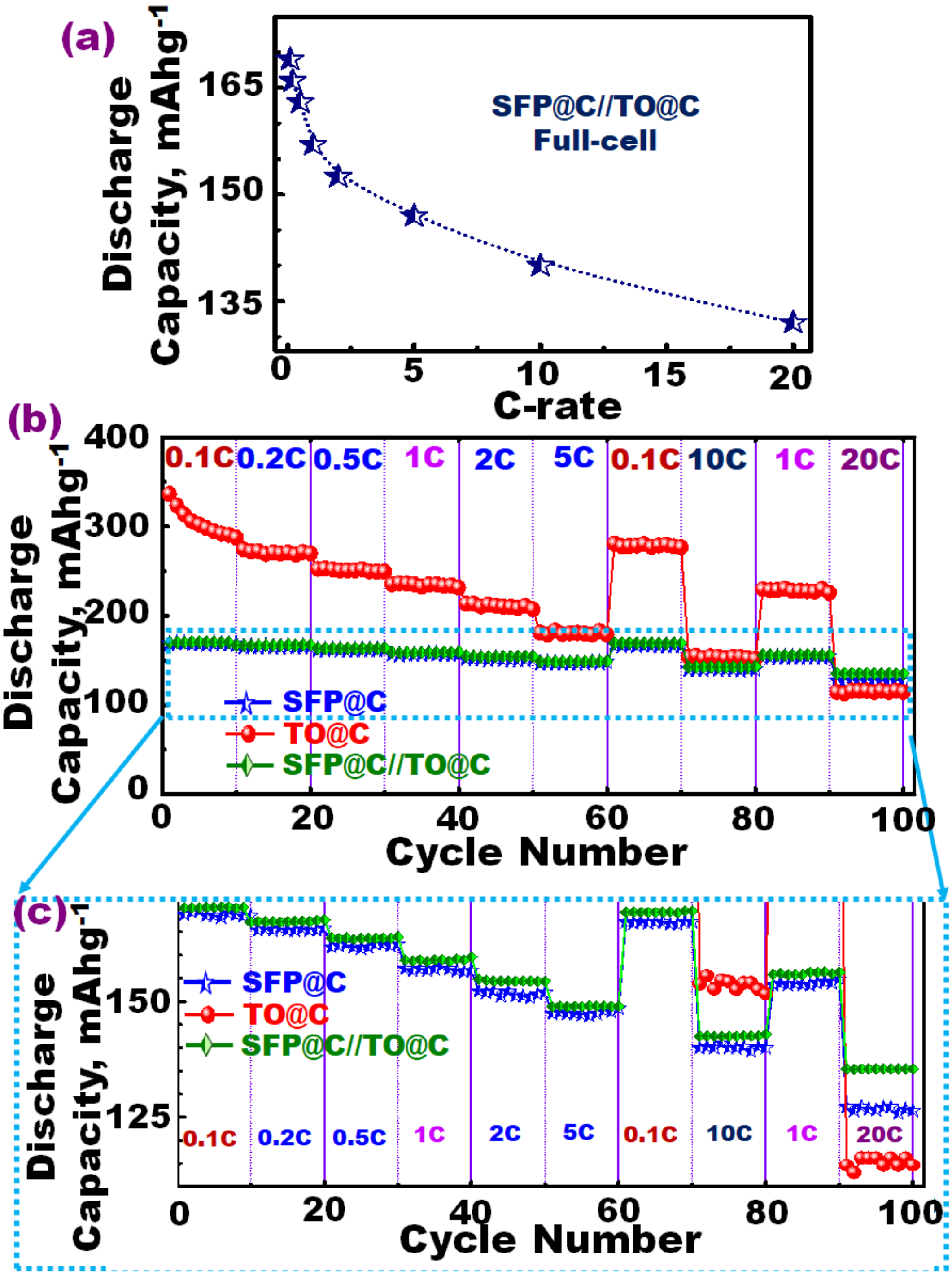

Fig. 6 (a) Behavior of specific discharge capacity in mAhg^{-1} versus current C-rates at 0.1C, 0.2C, 0.5C, 1C, 2C, 5C, 10C and 20C, and between voltage of 0.9 and 3.5 V for mesopolytope SFP@C // capsule 1D-TO@C LIB-CR2032-coin cell models. **(b)** Performance and behavior of the rate capability for mesopolytope SFP@C // capsule 1D-TO@C LIB-CR2032-coin cell models over a range of 0.9-3.5V at various current rates from 0.1C to 20C. **(C)** Enlarged the selected part of (b) for rate capability performance results of mesopolytope SFP@C // capsule 1D-TO@C LIB-

CR2032-coin cell models. All electrochemical measurements for full-cell LIB model were operated within voltage range of 0.9-3.5 V at 25 °C.

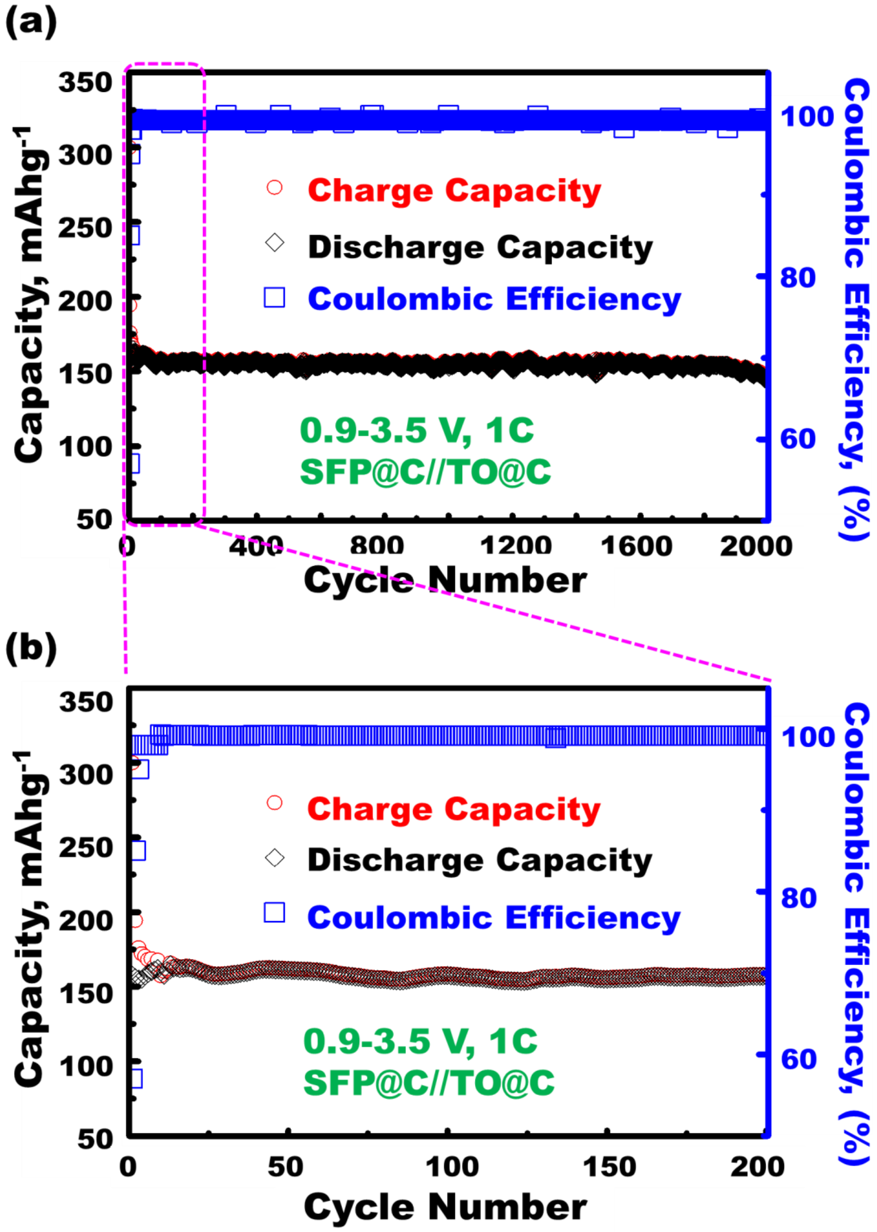

Fig. 7 (a) Long term cycling performance (stability) and Coulombic performance efficacy for mesopolytope SFP@C // capsule 1D-TO@C LIB-CR2032-coin cell models, at rate of 1C up to 2000 cycles, voltage range 0.9-3.5V, and at room temperature. **(b)** Enlarged cycling performance (stability) and Coulombic performance efficacy for mesopolytope SFP@C // capsule 1D-TO@C LIB-CR2032-coin cell models at rate of 1C up to 200 cycles.

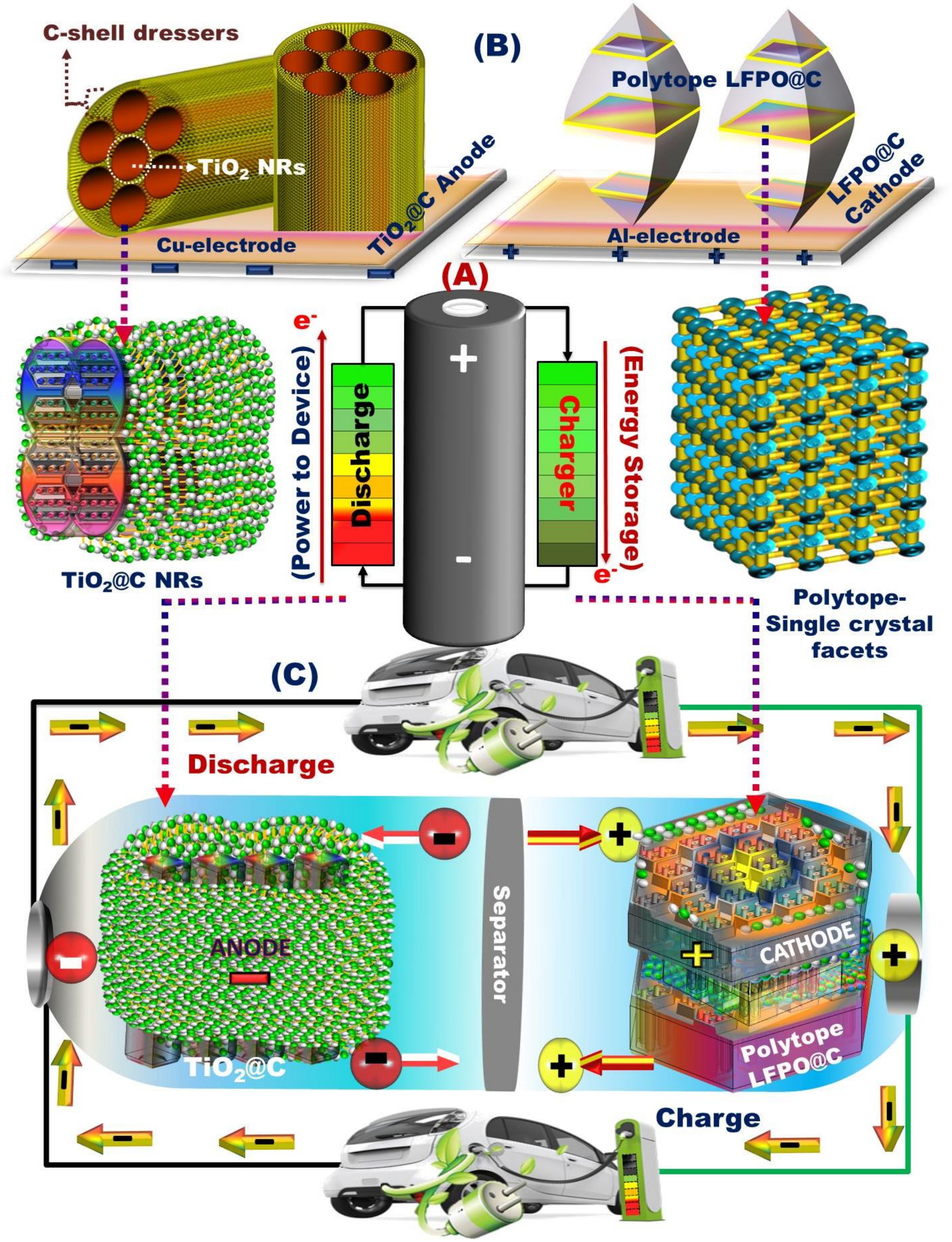

Scheme 1. Heterogeneous mesopolytope SFP@C // capsule 1D-TO@C LIB-CR2032-coin cells that packed-up in a collar fashion to form pouch-type LIB models for long term lithiation/delithiation cycling process (A-C) for possible application of electric vehicles (LIB-EVs). (B) The wrapping of full cell 1D-TO@C nanorod capsules (anode)// mesopolytope 3D-LFPO@C (3D-LFPO@C) (Cathode) electrodes. (C) Mechanistic Li-rechargeable battery during lithiation/delithiation cycling process of mesopolytope SFP@C // capsule 1D-TO@C CR2032-coin cells in pouch LIB models.

Multifaceted geometric 3D mesopolytope cathodes and its directional transport gates for superscalable LIB models

H. Khalifa, [a] S.A. El-Safty,*[a] A. Reda, [a] M.A. Shenashen, [a] A. Elmarakbi,[b] and H. Metawa, [a]

[a] National Institute for Materials Science (NIMS), Sengen 1-2-1, Tsukuba, Ibaraki 305-0047, Japan.

[b] Department of Mechanical & Construction Engineering, Faculty of Engineering and Environment, Northumbria University, Newcastle upon Tyne, NE1 8ST, UK.

E-mail: *sherif.elsafty@nims.go.jp*

Webpage: *https://samurai.nims.go.jp/profiles/sherif_elsafty*

S1. Materials, electrode synthesis and characterization

A- Chemicals used for fabrication of mesopolytope cathode and capsule anode

For the fabrication of fabrication of mesopolytope cathode and capsule anode materials, electrodes, and cells, all chemicals used are high-grade and purified. For example, lithium acetate dihydrate ($CH_3COOLi \cdot 2H_2O$), lithium chloride (LiCl), Iron II sulfate heptahydrate ($FeO_4S.7H_2O$), titanium (IV) ethoxide $Ti(OC_2H_5)_4$, hydrogen peroxide solution (H_2O_2) and ethanol(C_2H_5OH) were purchased from Sigma–Aldrich Company, Ltd., USA. Phosphoric acid (H_3PO_4) from Tokyo Chemical Industry (TCI) Company, Ltd., Tokyo, Japan. Ethylene glycol ($C_2H_6O_2$), and lithium hydroxide monohydrate ($LiOH.H_2O$), lithium nitrate ($LiNO_3$) and lithium carbonate (Li_2CO_3) from Nacali Tesque Company, Ltd., Kyoto, Japan. All the chemicals are quantitatively added in specific and stoichiometric ratios, materials 1D-TiO_2 anode and 3D-$LiFePO_4$ cathode compositions were synthesized by the hydrothermal methods (see below). Carbon coating process of 1D-TiO_2 and 3D-$LiFePO_4$ was done by microwave irradiation technique.

Fabrication of multi-faceted mesopolytope 3D-LFPO geometrics (cathode)

Anion-assisted synthesis and control formulation of multi-functional polytope LFPO building blocks of 16-faceted exposure polyhedron (SFP@C), octahedron simplex (OS@C), rhombus platelet (RP@C), parallelepiped complex object (PC@C), and convex complex (CC@C) mesopolytopes. For synthesis of LFPO 16-faceted polyhedron (SFP) structure; the LFPO component ratio of Li: Fe: P can be determined by rational addition of iron sulfate heptahydrate, phosphoric acid, and Li-anion compounds with equivalent ratio of 3:1:1. For real fabrication procedure, we have consequently made the fabrication pattern as follows: First step is the formation of composition solution. The components of phosphoric acid or iron sulfate heptahydrate were stirred for 1 hour in mixed solution of 5ml H_2O/ 5ml ethanol (C_2H_5OH)/ 2.5ml ethylene glycol ($C_2H_6O_2$). However Li-acetate dihydrate solution is formed in 10ml H_2O/ 10ml ethanol (C_2H_5OH)/ 5ml ethylene glycol ($C_2H_6O_2$) mixture under 1h stirring. Second step is the mixing the synthesis LFPO (SEP polytope) composition domains of Li: Fe: P. The phosphoric acid is added drop wise (with addition rate of 0.5ml/min) to the iron sulfate heptahydrate solution under 1h stirring. To this mixture, Li-acetate solution is also added under same rate conditions. Third step is growth seed SFP particles. The mixture domains of Li: Fe: P ratios at pH-7 are stirred for 6h. Fourth step is the formation of SFP polytope under hydrothermal treatment. The final mixture is transferred to autoclaves and treated at 170 °C for 12 h. The collected and dried powder products are calcined at high-temperature of 600^{o}C for 6 hours to fabricate single crystal of 16-facets polyhedron labeled as SFP. Using the similar four consequence fabrication procedures at pH-7, and composition ratios, the octahedron simplex (OS@C), rhombus platelet (RP@C), parallelepiped complex (PC@C), and convex complex (CC@C) mesopolytopes can be fabricated by using different Li-anion sources such as lithium chloride, lithium hydroxide monohydrate, lithium nitrate and lithium carbonate, respectively.

Fabrication of 1D-TiO_2-anatase (1D-TO) nanorod capsules (anode)

A homogenous solution of a mixture of 3 ml titanium (IV) ethoxide $Ti(OC_2H_5)_4$, 20ml milliQ-water, 20ml ethanol, 20ml HCl, and 300 mg thiouria is formed. To control the growth seed **1D-TO** particles, the homogenous domains at pH-9.2 is mixed with 4 ml H_2O_2 solution with addition rate of 0.5ml/min, and then the all mixture is stirred for 2h. To form the **1D-TO** nanorod geometrics, the hydrothermal treatment pattern at 170 °C for 12 h is used. The final power product is thermally treated at 600^{o}C for 3 hrs, leading to fabricate **1D-TO** nanorod geometric capsules.

Fabrication of the mesopolytope 3D-LFPO@C and 1D-TO@C capsules

The carbonization methodology of 3D-LFPO@C polytopes (cathodes) and 1D-TO@C capsules (anodes) was carried out by using microwave radiation technique using the following patterns. First, the powder materials are mixed with 5% w/w glucose as carbon source/15ml ethanol (C_2H_5OH) contents. Second, the heterogeneous mixture is treated under microwave irradiation using a temperature at 80 ^{o}C, and maintaining for 0.5 h under irradiation. Third, the resultant black precipitate is calcined in Ar atmosphere under the following thermally temperature pattern with heating rate 5^{o}C/min as follows; (i) treatment 350^{o}C for 0.5 h, and then (ii) following by high-temperature treatment set at 600^{o}C for 2 h. Under this simple procedure, the 3~5 nm carbon-shell dot-dressers are coated the outer surface layers of both anode and cathode materials without changes in the structural ordering, and atomic scale geometrics of resultant 1D-TO@C anode and polytope 3D-LFPO@C cathode materials.

Formulation of P- and N-electrodes and LIB cells

The 1D-TO-capsules and 3D-LFPO polytope-modified nanocarbon materials were used for fabrication of anode and cathode electrodes. Thus the these 1D-TO@C anode/cathode geometrics such as high-index, sixteen (16)-faceted polyhedron-crystal-structure SFP@C, octahedron simplex (OS@C), rhombus platelet (RP@C), parallelepiped complex object (PC@C), and convex complex (CC@C) polytopes are used in fabrication of half-, full-, and large-scale LIB models.

B- Characterization of mesopolytope cathode and capsule anode

To investigate the crystal structures of both 1D-TiO_2@C nanorods-like capsules (anode) // 3D-$LiFePO_4$@C mesopolytope cathode composites, X-ray diffraction (XRD) characterization was performed by using a 18 kW diffractometer (Bruker D8 Advance X-ray diffractometer).

The microscopic patterns of 1D-TiO_2@C nanorods-like capsules (anode) and 3D-$LiFePO_4$@C cathodes with heterogeneous high-index, homeomorphic sixteen-faceted exposure polyhedron (SFP@C), octahedron simplex (OS@C), rhombus platelet (RP@C), parallelepiped complex object (PC@C), and convex complex (CC@C) mesopolytopes were investigated by the following techniques: (1) Field emission-type Scanning electron microscope FE-SEM (Jeol JSM-Model 7000F, JEOL Ltd) at 20 kV. (2) In addition to FE-SEM, the geometric structures were investigated by high-resolution transmission electron microscopy (HRTEM) images, electron diffraction (ED), scanning transmission electron microscopy (STEM). These HRTEM/ED/STEM techniques were performed at atomic-level imaging, structural and chemical analysis field emission-type TEM (JEM-ARM200F) at 200 kV using machine model of JEOL 2100F, JEOL Ltd.

The textural surface properties such as pore size distribution and surface area of LFPO@C (cathode) mesopolytope building blocks with heterogeneous high-index, homeomorphic sixteen-faceted exposure polyhedron (SFP@C), octahedron simplex (OS@C), rhombus platelet (RP@C), parallelepiped complex object (PC@C), and convex complex (CC@C) mesopolytopes and 1D TO@C nanorod-like capsules is estimated by N_2 isotherms at 77 K using a BELSORP36 analyzer (JP. BEL Co., Ltd.).

The thermal stability of LFPO@C mesopolytopes (cathode) and TO@C NR capsules (anode) is crucial for establish outstanding cycling performance, stability and Coulombic efficiency for 3D super-scalable mesopolytope-built-in SFP@C//TO@C full-scale LIB-model under wide range of temperatures and after numerous cycles (ageless life time). To investigate the thermal stability of cathode//anode samples, the weight content loss of heterogeneous mesopolytope building blocks cathode composites were determined from the weight loss curve measured under simulated air atmosphere on thermo-gravimetric and differential scanning calorimetry (TG/DSC) instrument TG/DSC-60 (Shimadzu, Japan) with a heating rate of 10 ^{0}C min^{-1}.

X-ray photoelectron spectroscopy (XPS) analysis (0-1400eV) using Perkin–Elmer Co., USA, Raman spectroscopy (HR Micro Raman spectrometer, Horiba, Jobin Yvon), and Fourier transform infrared spectroscopy (ATR-FTIR, Spectrum 100, Perkin-Elmer, Inc., USA), respectively, are used for surface characterization of . 3D-LFPO@C (cathode) mesopolytopes with heterogeneous high-index, homeomorphic sixteen-faceted exposure polyhedron (SFP@C), octahedron simplex (OS@C), rhombus platelet (RP@C), parallelepiped complex object (PC@C), and convex complex (CC@C) mesopolytopes and 1D TO@C nanorod-like capsules (anode).

C- Control design of polytope LFPO@C (cathode) and TO@C capsules (anode) CR2032-coin LIB formulations

All consumed chemicals for new generation of heterogeneous mesopolytope 3D LFPO@C// capsule 1D-TO@C full-scale LIB-model, half-scale 1D-TO@C capsule LIB-anode model, and half-scale 3D-LFPO@C mesopolytope LIB-cathode model have high analytical grade and without further purification. For example, lithium hexafluoro-phosphate $LiPF_6$, carbon black and polyvinylidene fluoride (PVDF) are from Sigma–Aldrich Company, Ltd., USA. N-methyl-2-pyrrolidone (NMP) from Tokyo Chemical Industry (TCI) Company, Ltd., Tokyo, Japan. To carry out the electrochemical measurements, the Li-ion intercalation was performed using CR2032 coin-cells that assembled in a glovebox under pure Ar-gas (see Figure S1).

Within a design of half-scale 1D-TO@C capsule LIB-anode model, and half-scale 3D-LFPO@C mesopolytope LIB-cathode model, we used Lithium foil used as reference and counter electrode to control the electrochemical performances of the half-scale 1D-TO@C capsule LIB-anode model and half-scale 3D-LFPO@C (i.e., SFP@C, OS@C, RP@C, PC@C and CC@C and TO@C) mesopolytope LIB-cathode models. In turn, we designed 1D-TO@C//3D-SFP@C as anode//cathode full-cell CR2032-coin LIB formulations for electrochemical measurements of full-scale LIB-EV model system (Figure S1).

In order to fabricate the 3D-LFPO@C cathode // 1D-TO@C anode full-scale LIB-model, half-scale 1D-TO@C capsule LIB-anode model, and half-scale 3D-LFPO@C mesopolytope LIB-cathode CR2032-type coin cells, the liquid electrolyte prepared as a solution of $LiPF_6$ (1 M) conductive salt in ethylene carbonate/diethyl carbonate (1:1 v/v). In addition, to fabricate mesopolytope 3D-LFPO@C and capsule 1D-TO@C in P- and N-working electrodes, we used a mixture of 1D-TO@C capsule anode or 3D-LFPO@C polytope cathode materials/ carbon-black/polyvinylidene fluoride (PVDF) with equivalent mass ratio of 75:15:10, respectively. To fabricate the active material slurries, a rational amount of N-methyl-2-pyrrolidone (NMP) solvent is added with 1 h stirring. The working electrodes are prepared by mixing each active slurry of mesopolytope 3D-LFPO@C and capsule 1D-TO@C (i.e., cathodic and anodic materials) into 10 µm-aluminum (Al) and 8 µm-cupper (Cu) foils. The loading amount (i.e., mass/electrode area) of the active1D-TO@C capsule anode or 3D-LFPO@C polytope cathode materials into 8 µm-Cu or 8 µm-Al foils is 6.63 and 13.14 mg/cm^{-2}

To investigate the electrochemical performance of the 3D-LFPO@C cathode // 1D-TO@C anode full-scale LIB-model, half-scale 1D-TO@C capsule LIB-anode model, and half-scale 3D-LFPO@C mesopolytope LIB-cathode CR2032-type coin cells in terms of galvanostatic charge/discharge characteristics, we used multichannel battery system (LAND CT2001A, Wuhan, China). Cyclic voltammetry (CV) measurements of 3D-LFPO@C cathode // 1D-TO@C anode full-scale LIB-model, half-scale 1D-TO@C capsule LIB-anode model, and half-scale 3D-LFPO@C mesopolytope LIB-cathode CR2032-type coin cells are also tested using (CHI 660c electrochemical workstation). Electrochemical impedance spectroscopy (EIS) was performed using (Zennium/ZAHNER-Elektrik GmbH & CoKG, controlled by Thales Z-3.0 software–frequency range from 0.1 Hz to 1 MHz). ZS-102 tap density meter was used measure the tap density of the electrodes. EIS (electrochemical impedance spectroscopy) results can be illustrated on the basis of its equivalent circuit, which is consisted of electrolyte resistance (R_s), charge transfer resistance (R_{ct}), and Warburg impedance of representative Li^+-ion transport along mesopolytope electrodes (W_f), respectively. All the electrochemical performance measurements were done at 25 ^oC.

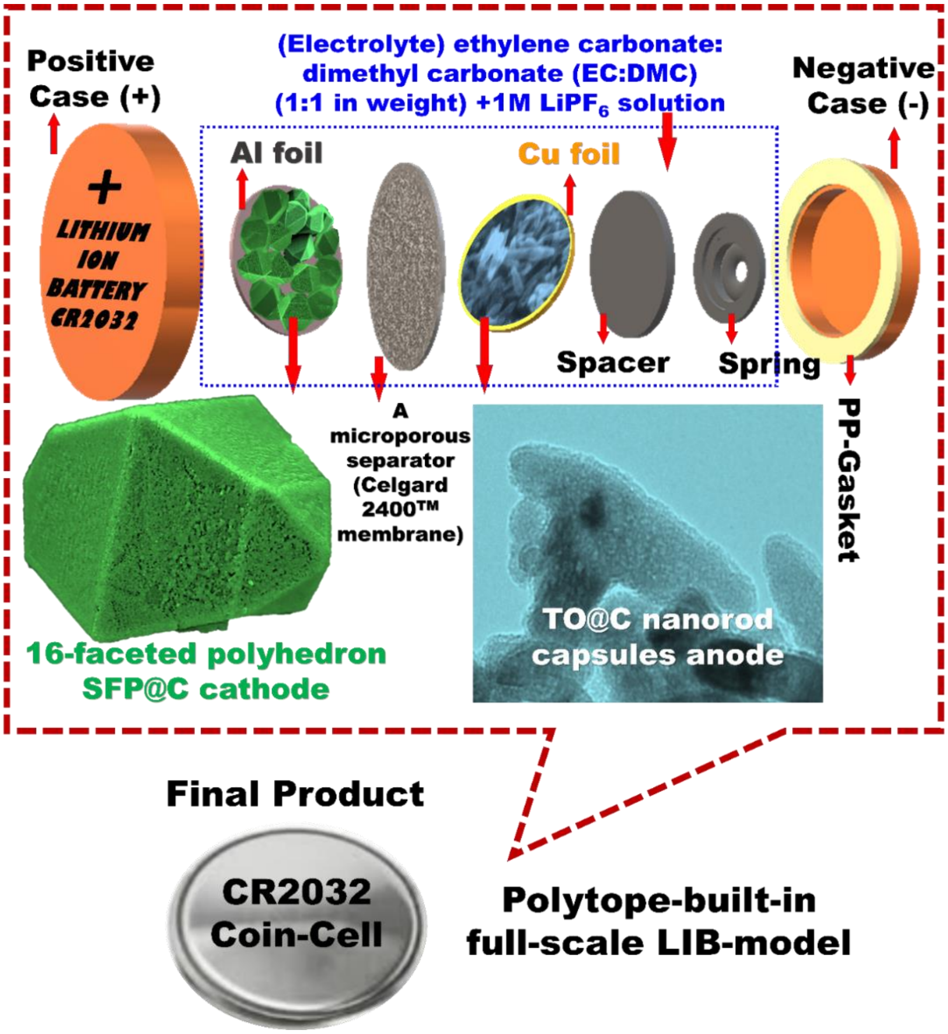

Fig. S1. (a) Illustration of the 3D-LFPO@C cathode // 1D-TO@C anode full-scale LIB-model, half-scale 1D-TO@C capsule LIB-anode model, and half-scale 3D-LFPO@C mesopolytope LIB-cathode CR2032-type coin-cell models.

S2-S5 Characterization of mesopolytope 3D-LFPO@C geometrics

The morphologies of large-scale 3D-LFPO@C mesopolytopes with heterogeneous high-index, homeomorphic octahedron simplex (OS@C), rhombus platelet (RP@C), parallelepiped complex object (PC@C), and convex complex (CC@C) mesopolytopes of variable model geometrics and multifaceted exposure sites were investigated using FE-SEM, EDS and HR-TEM pattern images for prepared hierarchy samples as shown in Figs S2, S3, S4 and S5; respectively. The morphologies of parent heterogeneous high-index, homeomorphic sixteen-faceted exposure polyhedron (SFP@C), octahedron simplex (OS@C), rhombus platelet (RP@C), parallelepiped complex object (PC@C), and convex complex (CC@C) mesopolytopes with variable model geometrics and multifaceted exposure sites were investigated using low and high magnification FE-SEM, EDS and HR-TEM images for prepared hierarchy samples as shown in Figs; S2 (a-b) and S3(a-c), respectively.

The crystal structures of large-scale mesopolytope building blocks with heterogeneous mesopolytopes of variable model geometrics and multifaceted exposure sites were further analyzed by HR-TEM as shown in Figs. [S2(d-f), S3(e-g), S4(d-f) and S5(e-g)]; respectively. All samples exhibit evident crystal planes with interatomic spacing of [(0.39,0.98), (0.41,1.01) (0.39,1.01) and (0.39,1.03) nm, identical to (001) and (100) planes of orthorhombic polytope building blocks as cathode composites; respectively. SAED pattern images of OS@C, RP@C, PC@C and CC@C particles can be shown in Figs.[S1(f), S2(g), S3(f) and S4(g)]; respectively. It is evident that, exposed [010] ac-plane are prominent for as prepared heterogeneous polytope building blocks. The low surface energy of [010] plane led to form stable direction and orientation on surface topology than that of the other crystal planes, indicating that the [010] plane is suitable surface for Li^+ ion diffusion and accommodation.

HR-TEM lattice pattern images (Figs. [S2(e), S3(f), S4(e) and S5(f)]) show clear, thin and smoothed layer 4-5 nm of C-coating at the surface edge on prepared particles which has been characterized by Raman spectra, supporting information (Fig. S8). Our finding indicates that surface coating of prepared polytope materials with highly conductive C dots facilitates electron/ion transports that improve the electronic conductivity and ionic diffusion dynamics. Moreover, capsulate the electrode material with thin layer of conductive C increases the stability of the integral hierarchy structured heterogeneous mesopolytope building blocks as cathode composites structures with within high rate cycling. Energy-dispersive X-ray spectroscopy (STEM-EDS) was performed with high-resolution elemental mapping to investigate Composition distribution of the composite chemical contents along the nanostructures morphological hierarchy OS@C, RP@C, PC@C and CC@C unit blocks by using a 200 kV TEM (JEOL 2100F, JEOL Ltd) field emission-type transmission electron gun microscope as shown in Fig. S2(c), S3(d), S4(c) and S5(d). HR-TEM and STEM-EDS results indicate the purity of OS@C, RP@C, PC@C and CC@C samples as pure olivine orthomorphic mesopolytope building blocks as cathode composites with no present of other foreign elements.

S2. Morphological structure of octahedron structure (OS@C) geometrics

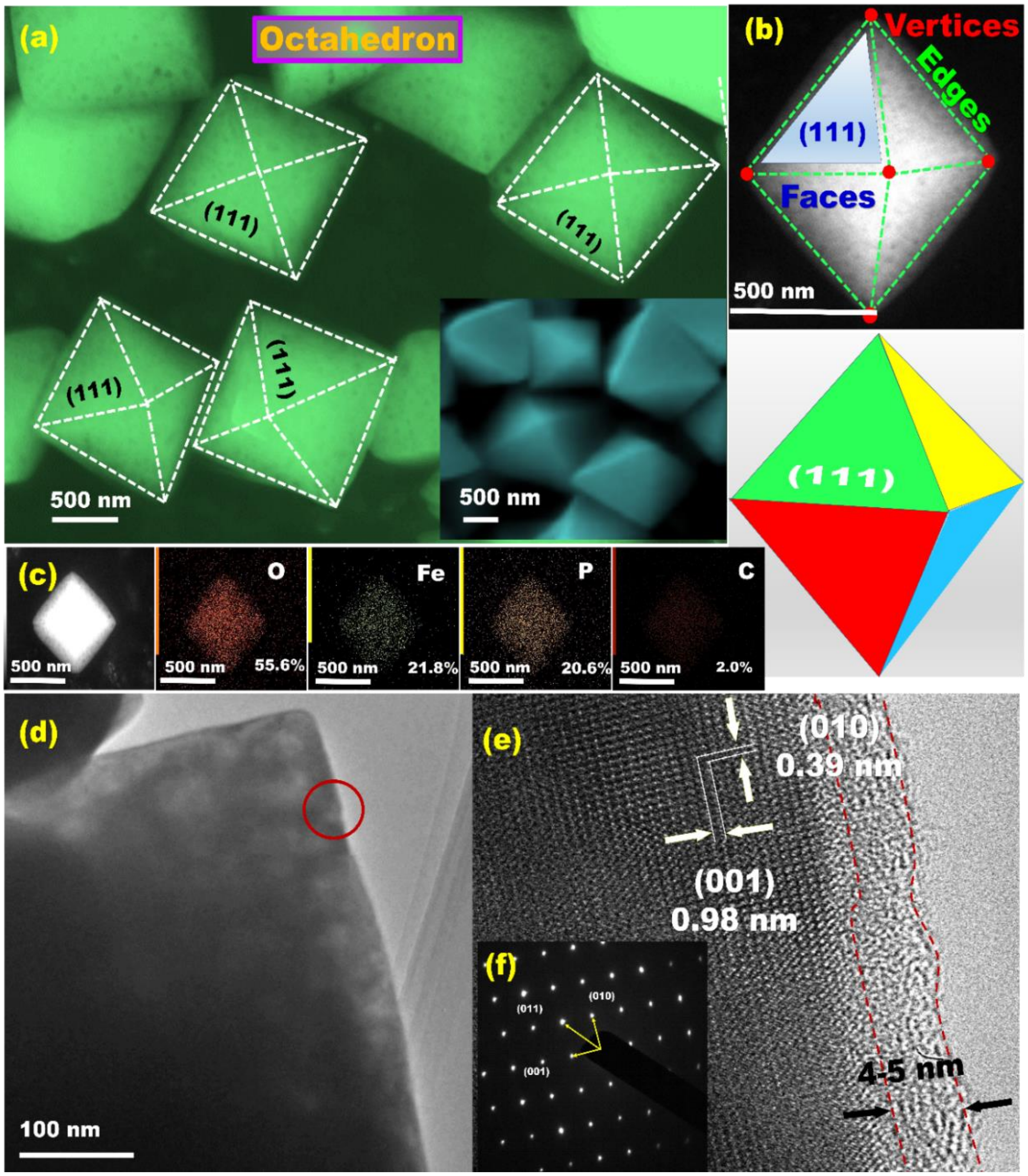

Fig. S2 (a) and (b) High magnification of FE-SEM for heterogeneous mesopolytopes as cathode with a 3-D cross-polytope octahedron simplex (OS) (i.e., eight faces, twelve edges, and six vertices) and exposed {111} facets labeled as (OS@C). **(c)** Elemental mapping of OS@C. (**d, e and f)** HR-TEM micrographs with low and high magnifications. **(e)** The lattice pattern at edge with clear thin layer 4-5 nm of C-coating on surface of OS particle. **(f)** Selected area electron diffraction (SAED) pattern image of OS@C unit block with incident beam along the [111] crystallographic direction indicates the single crystal of OS@C geometrics.

S3. Morphological structure of rhombus platelets (RP@C) geometrics

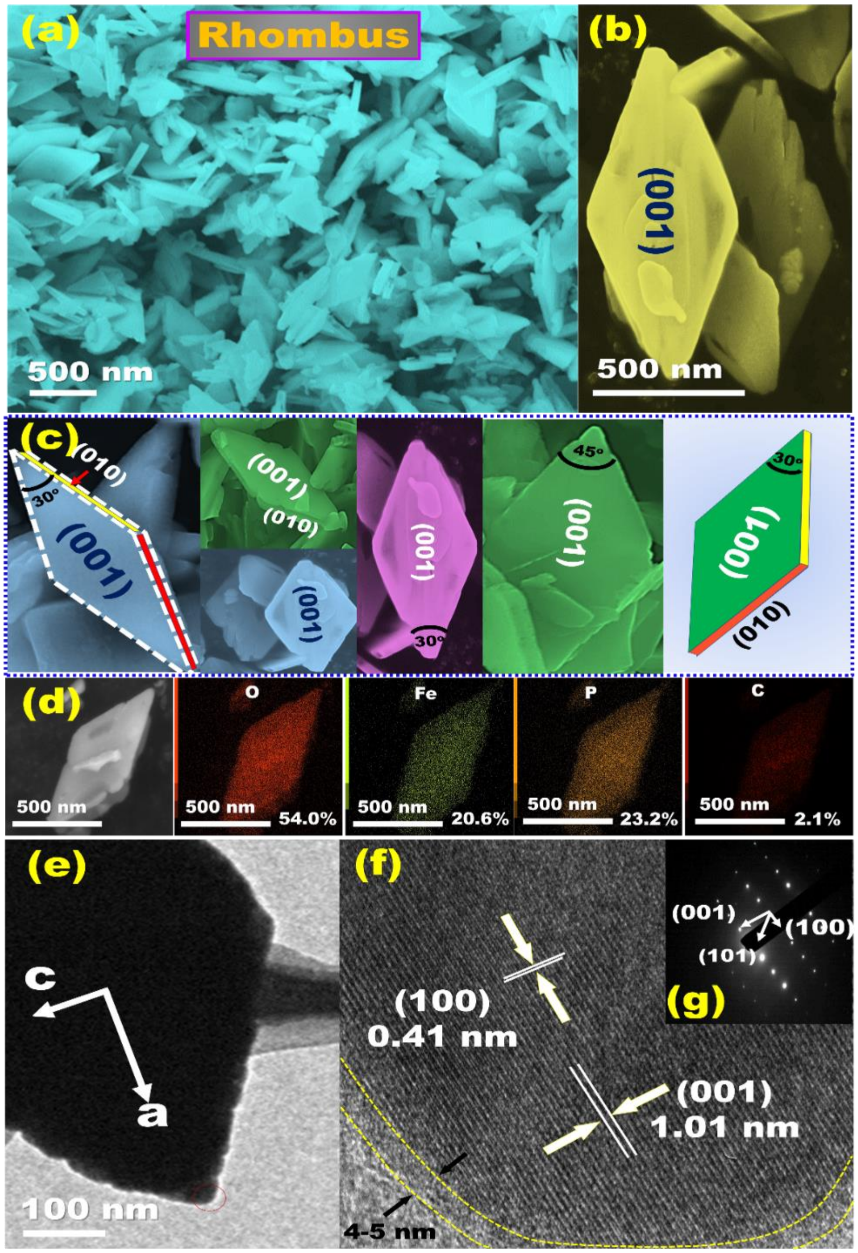

Fig. S3 (a), (b and c) Low and high magnifications of FE-SEM for heterogeneous mesopolytopes as cathode with rhombus platelets particles -like morphological and exposed [010] facets labeled as (RP@C). **(d)** Elemental mapping of RP@C. (**e, f and g)** HR-TEM micrographs with low and high magnifications. **(f)** The lattice pattern at edge with clear thin layer 4-5 nm of C-coating on surface of RP particle. **(g)** Selected area electron diffraction (SAED) pattern image of RP@C unit block with incident beam along the [010] crystallographic direction indicates the single crystal of RP@C geometrics.

S4 Morphological structure of parallelepiped complex structure (PC@C) complex geometrics

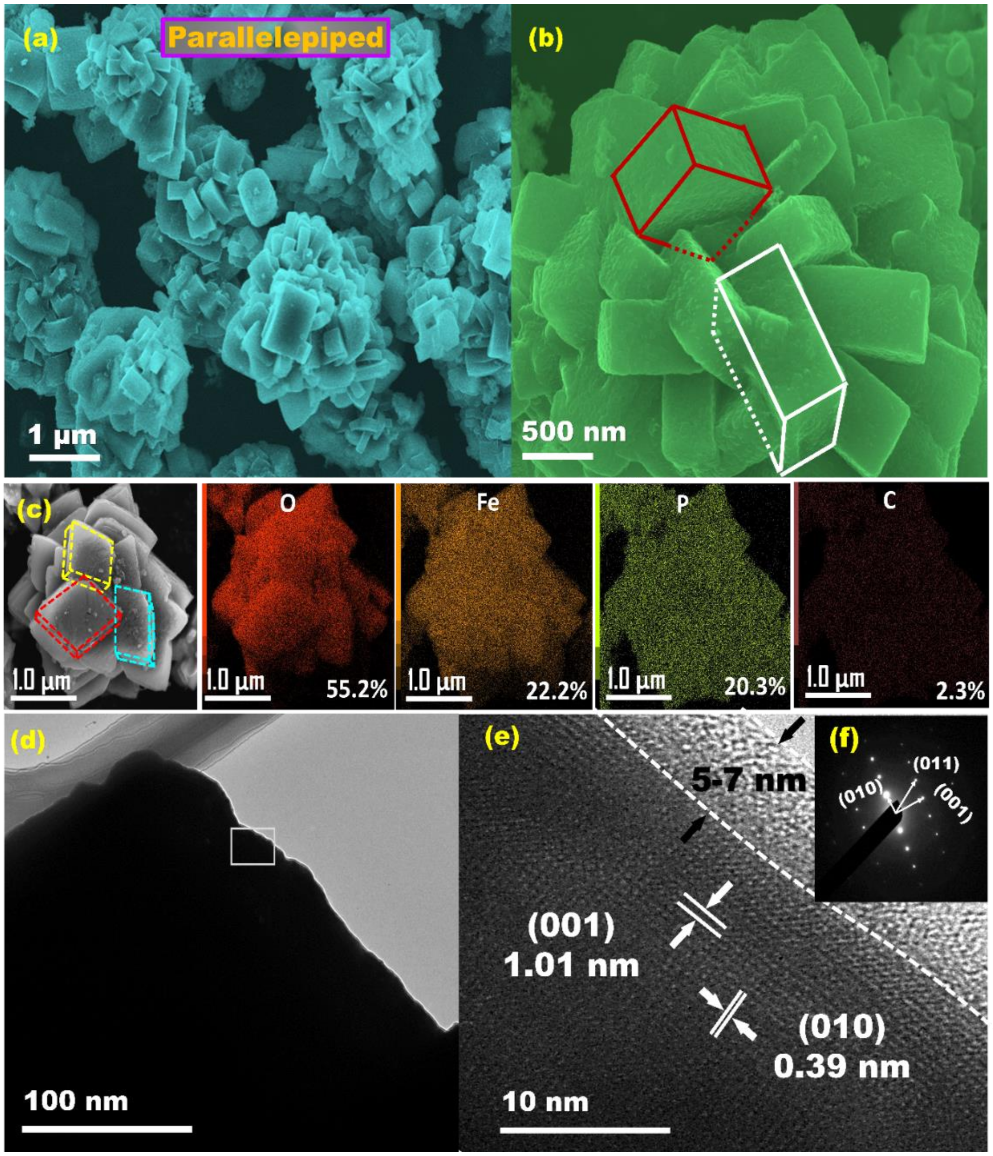

Fig. S4 (a) and (b) Low and high magnifications of FE-SEM for heterogeneous mesopolytopes as cathode composites with parallelepiped complex structure (PC@C). **(c)** Elemental mapping of PC@C. **(d, e and f)** HR-TEM micrographs with low and high magnifications. **(e)** The lattice pattern at edge with clear thin layer 5-7 nm of C-coating on surface of PC particle. **(f)** Selected area electron diffraction (SAED) pattern image of PC@C unit block with incident beam along the [100] crystallographic direction indicates the single crystal of PC@C geometrics.

S5. Morphological structure of cuboid complex structure (CC@C) complex

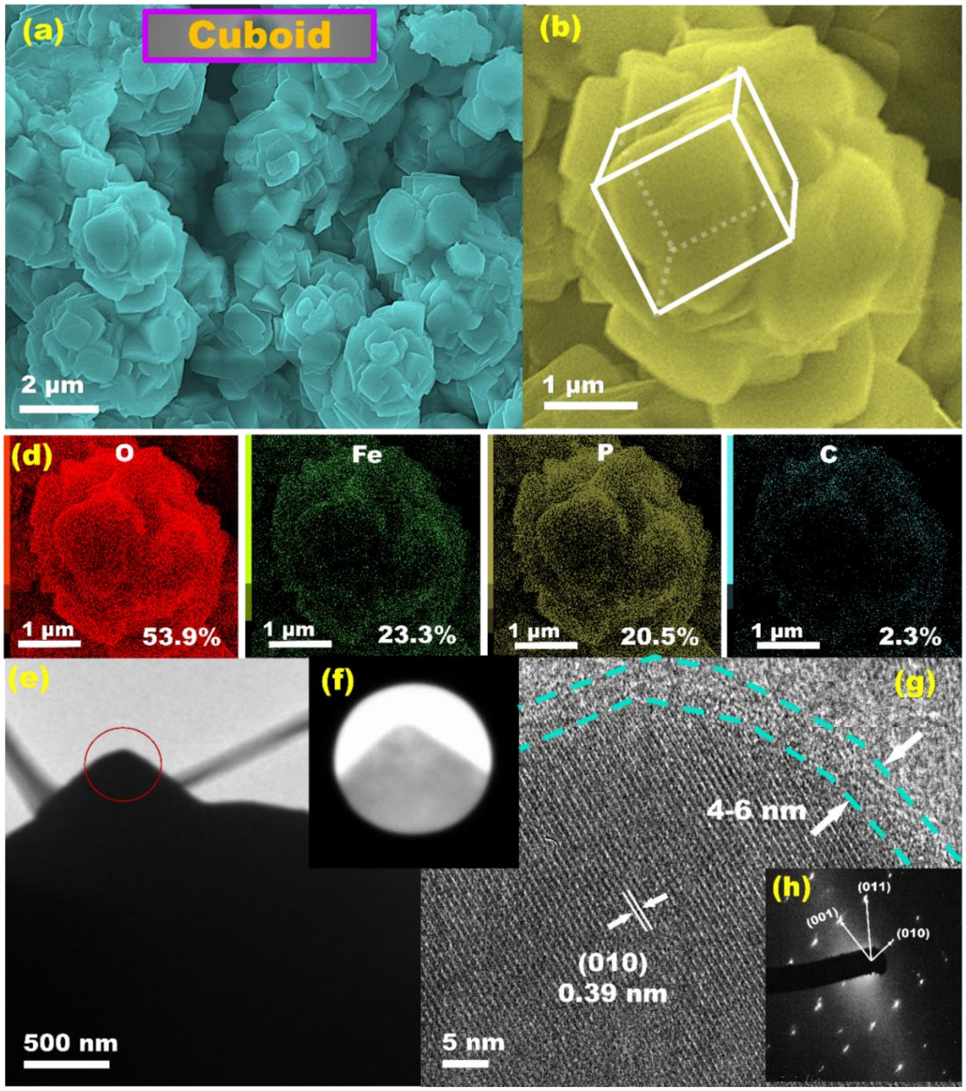

Fig. S5 (a), and (b) Low and high magnifications of FE-SEM for heterogeneous complex mesopolytopes as cathodes with dominated convex complex polytopes (CC@C), combinatorial manifolds of simple geometric polygons such as triangle, cuboid, pyramid, and tehrahedra objects that formed disjoint edges and vertices in non- homogeneous coordinates. **(d)** Elemental mapping of CC@C. **(e, f, g and h)** HR-TEM micrographs with low and high magnifications. **(g)** The lattice pattern at edge with clear thin layer 4-6 nm of C-coating on surface of CC particle. **(h)** Selected area electron diffraction (SAED) pattern image of CC@C unit block with incident beam along the [100] crystallographic direction indicates the single crystal of CC@C geometrics.

S6. Thermal Stability of mesopolytope 3D-LFPO@C cathodes

TG/DSC measurements were performed to 3D-LFPO@C polytope architects cathodes using TG-60 (Shimadzu, Japan) instrument with a heating rate of 10 °C min^{-1}. Thermal stability and loss in weight content of large-scale mesopolytope building blocks with heterogeneous SFP@C, OS@C, RP@C, PC@C, and CC@C cathode composites are clearly observed by TG/DSC analyses, Fig. S6. The TG and DSC curves of the tested cathode composites are similar with all polytope cathodic samples. Three discrete regions of weight loss or heat transfer were found under the temperature ranges 0-1000 °C. The weight loss or heat transfer region below 350°C is due to the releasing of absorbed water and chemisorbed crystal water (desorption of water). The second weight loss or heat transfer region is from 350°C to 550°C for the SFP@C, OS@C, RP@C, PC@C, and CC@C mesopolytopes indicates the endothermic effects of heating C-shell-dressers onto cathodic LFPO@C samples. The third weight loss or heat transfer region above >> 600°C is due to the exothermic crystallization peaks of 3D-LFPO@C polytope architects.

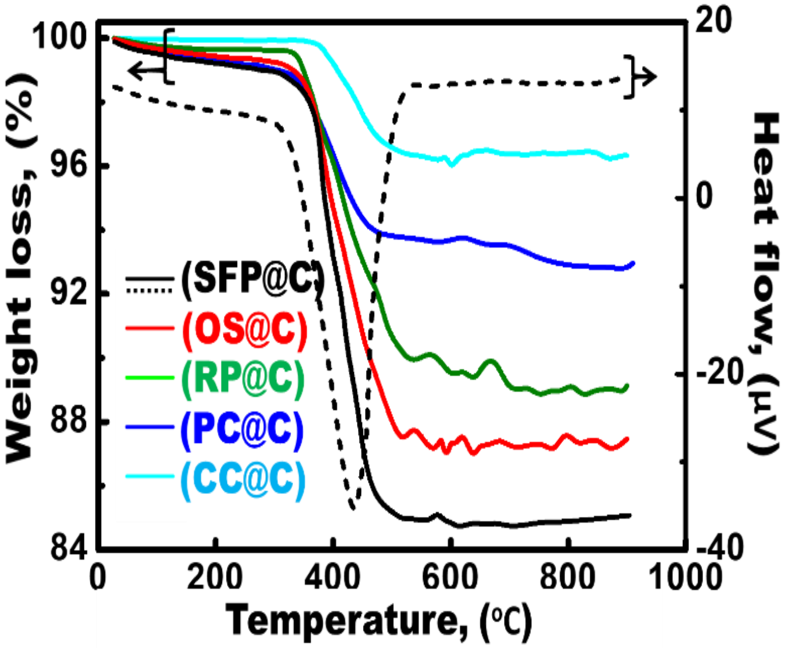

Fig. S6 TG-DSC curves of the different large-scale mesopolytopes with heterogeneous high-index, homeomorphic SFP@C, OS@C, RP@C, PC@C, and CC@C cathode composites.

S7. Chemical structure of 3D-LFPO@C mesopolytope cathodes

The chemical compositions and framework structure of the SFP@C, OS@C, RP@C, PC@C and CC@C cathode materials were investigated by Fourier transform infrared spectroscopy. Fourier transform infrared (FT-IR) spectra were performed to polytope SFP@C samples, Fig. S7. FT-IR spectrum of SFP@C exhibits a peak at 578 cm^{-1}, small intense peak around 1440 cm^{-1} and peak at 3250 cm^{-1} that attributed to Fe−O, P−C and C=H2 stretching vibrations. Strong band centered at 1090 cm^{-1} is ascribed to −CPO$_3$ group tetrahedral stretching vibration. The weak peak at 1536 cm^{-1} is due to C=H2 bending vibration. Our finding indicates the formation of Fe-P framework with LFPO materials. The C-coated materials exhibit characteristic peaks (see star marks), which is belonging to aromatic oxides at 1615 and 1718 cm^{-1}, respectively. The finding indicates the formation of C=O stretching with the LFPO structures.

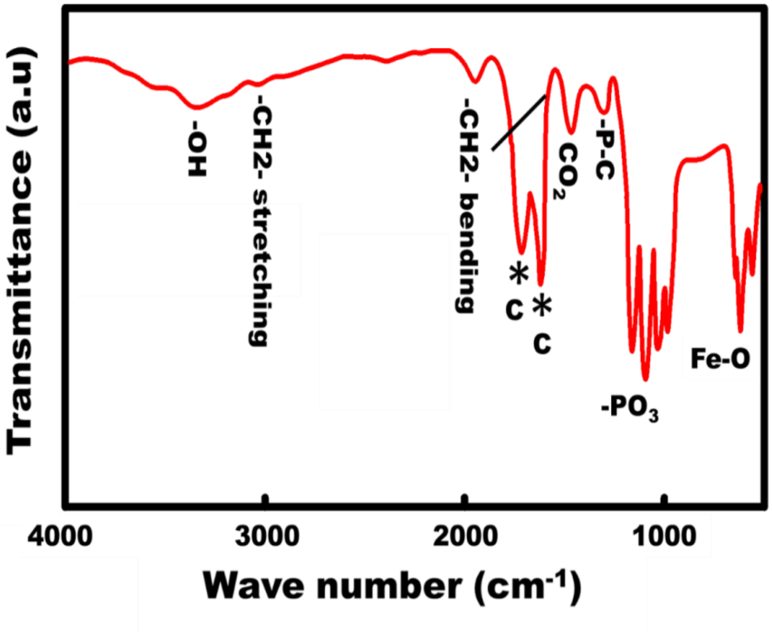

Fig. S7 FT-IR spectra of 3D-LFPO@C with sixteen-faceted exposure polyhedron (SFP@C), octahedron simplex (OS@C), rhombus platelet (RP@C), parallelepiped complex object (PC@C), and convex complex (CC@C) mesopolytopes.

S8. Framework structures of 3D-LFPO mesopolytope geometrics

Raman spectroscopy results for SFP@C polytope are shown in **Fig.S8. (a** and **b)**. The bands at 640.0 and 940.6 cm^{-1} indicate the symmetric modes of ofide forms (Fe_3O_4) and (PO_4^{3-}) groups oriented in the framework of 6-faceted exposure polyhedron (SFP@C) polytope. The appearance of these bands under Raman conditions indicates that the ~5 nm C-shell dot-dressers coated the outer surface SFP@C layers are very thin enough to enable the penetration of the laser beam. Two peaks revealed at 1342.63 and 1588.52 cm^{-1} are attributed to D and G bands of carbon in 3D-LFPO mesopolytopes (such as SFP@C, OS@C, RP@C, PC@C, and CC@C structures), respectively. The C-D-peak resolutions indicate the formation disordered C-shell dot-dressers with highly defective graphite structures. The C-G-peak resolutions indicate the formation of graphite structures with orientation of in-plane vibrations with E_{2g} symmetry. Our finding indicate that the ~5 nm C-shell dot-dressers coated the outer surface SFP@C layers may occurred throughout the cross-linking bonds of C=C, C=N, C=O, respectively.

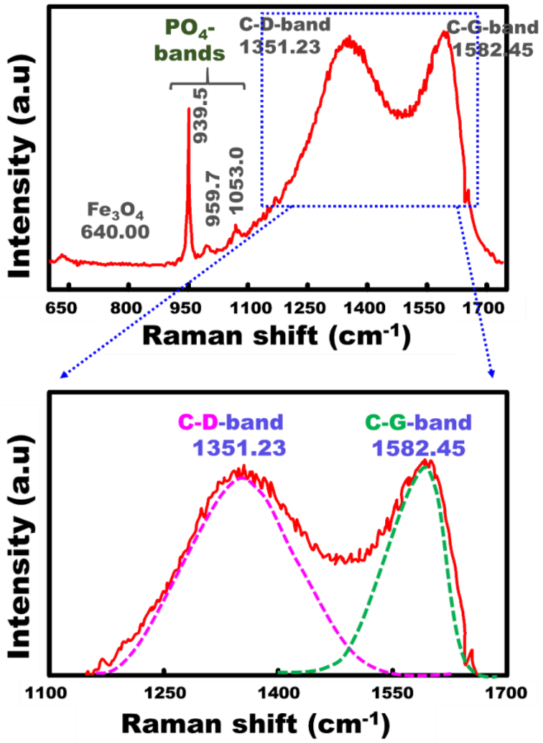

Fig. S8. (a and **b)** Raman spectra of 3D-LFPO mesopolytopes such as SFP@C, OS@C, RP@C, PC@C, and CC@C structures.

S9. Surface binding and chemical composition of 3D-LFPO mesopolytope geometrics

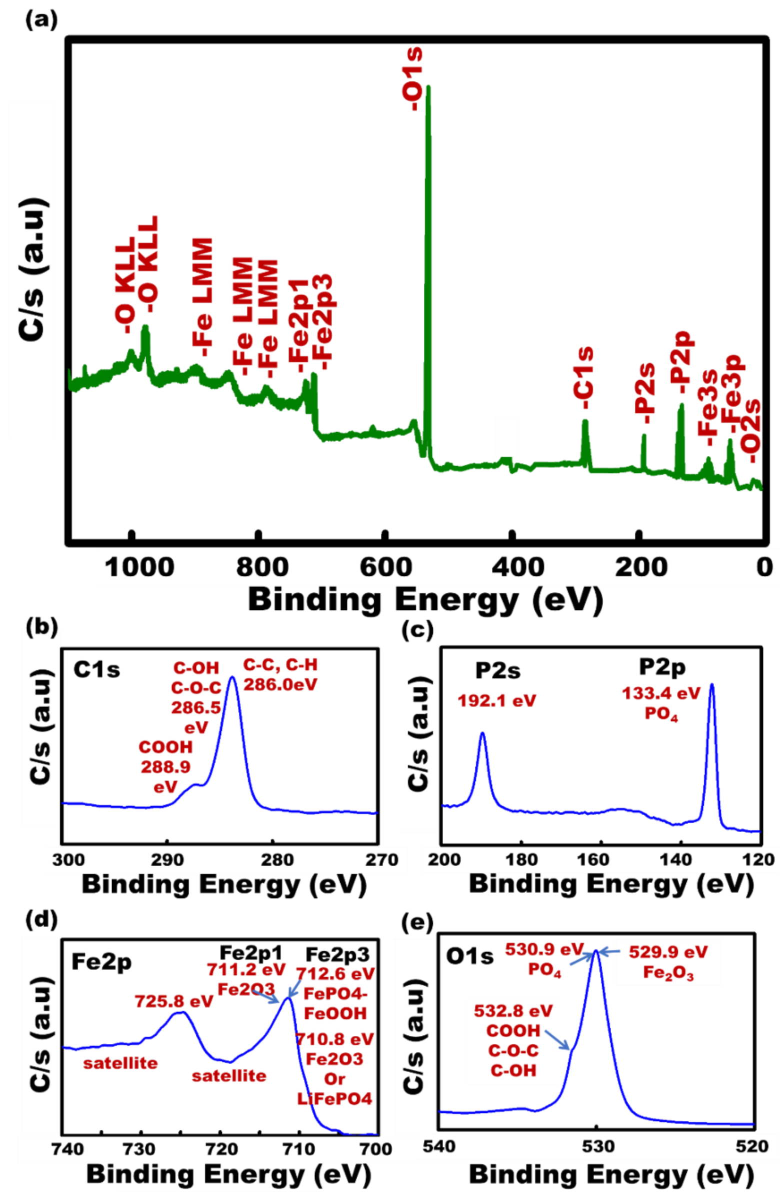

Fig. S9 X-ray photoelectron spectroscopy (XPS) analysis and survey spectrum of 3D-LFPO mesopolytopes such as SFP@C, OS@C, RP@C, PC@C, and CC@C structures

XPS spectrum provides the sensitive surface information in terms of compositions, oxidation states and valences of SFP@C polytopes, Fig. S9. The XPS spectral peaks at 711.2 and 530.9 eV are assigned to the (BEs) binding energies of Fe2p and O1s, respectively. The Fe-BE is related only to its valence state (Fe^{2+}) without interference by other valence states. The BEs of P2p, Li1s and C1s peaks are shown at

133.4, eV 55.8 and 284.9 eV, respectively. XPS results indicate that the high-index, sixteen (16)-faceted polyhedron-crystal-structure SFP@C polytope composites are consisted of all elements of olivine 3D-$LiFePO_4$@C polytopes, in agreement with XRD profiles.

Together, the XPS, Raman spectroscopy, and FTIR analyses indicate the following findings:

i. The formulation of 3D-LFPO polytope-modified nanocarbon architectures, such as high-index, sixteen (16)-faceted polyhedron-crystal-structure SFP@C, octahedron simplex (OS@C), rhombus platelet (RP@C), parallelepiped complex object (PC@C), and convex complex (CC@C) polytopes, which are used as cathodes in half-, full-, and large-scale LIB models.

ii. The multi-functional heterogeneous anode/cathode materials via coating of nano-carbon layers onto their outer surfaces.

iii. The thermal, chemical and physical stability of homeomorphic sixteen-faceted exposure polyhedron (SFP@C), octahedron simplex (OS@C), rhombus platelet (RP@C), parallelepiped complex object (PC@C), and convex complex (CC@C) mesopolytopes,

iv. The formation of variable model geometrics with superscalable mesopolytope 3D-LFPO@C crystal facets that have multifaceted exposure sites and anisotropic surface topologies.

v. The multi-functional surface composites, reactively heterogeneous high-index components, active surface mobility sites are probably responsible for efficient electrochemical performances of fabricated polytope 3D-LFPO@C cathode // capsule TO@C anode full-scale LIB-CR2032 coin-cell models, and both half-scales of 1D-TO@C capsule LIB-anode, and 3D-LFPO@C LIB-cathode model cells.

S10. Crystal structure formation of capsule 1D-TO@C

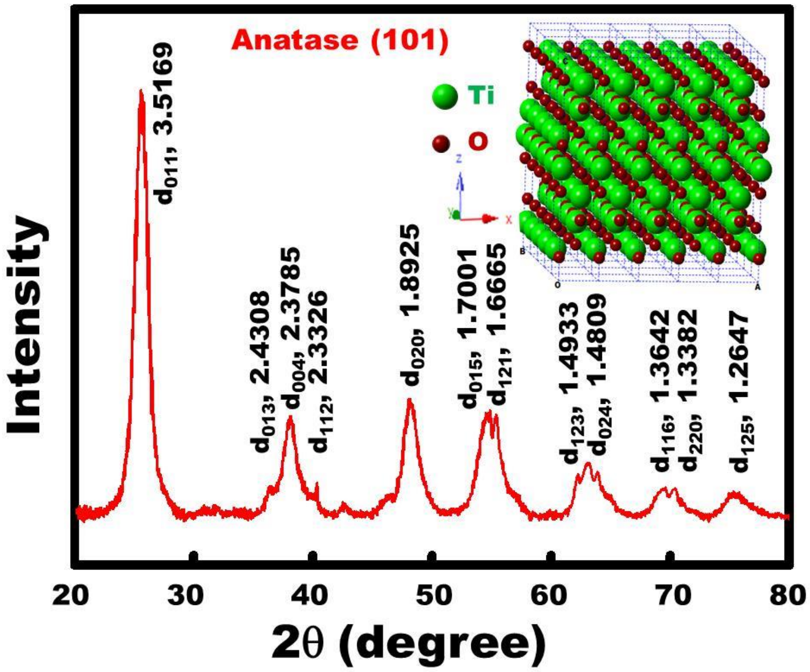

Fig. S10 XRD patterns of the capsule 1D-TO@C anode in half-cell LIB. **(Inset)** Anatase crystal structure with the I41/amd symmetry group oriented along [101]-plane direction.

S11. Effective 3D LFPO@C cathode model geometrics in the long-period stability of half-scale cathode LIB-CR2032 coin-cells

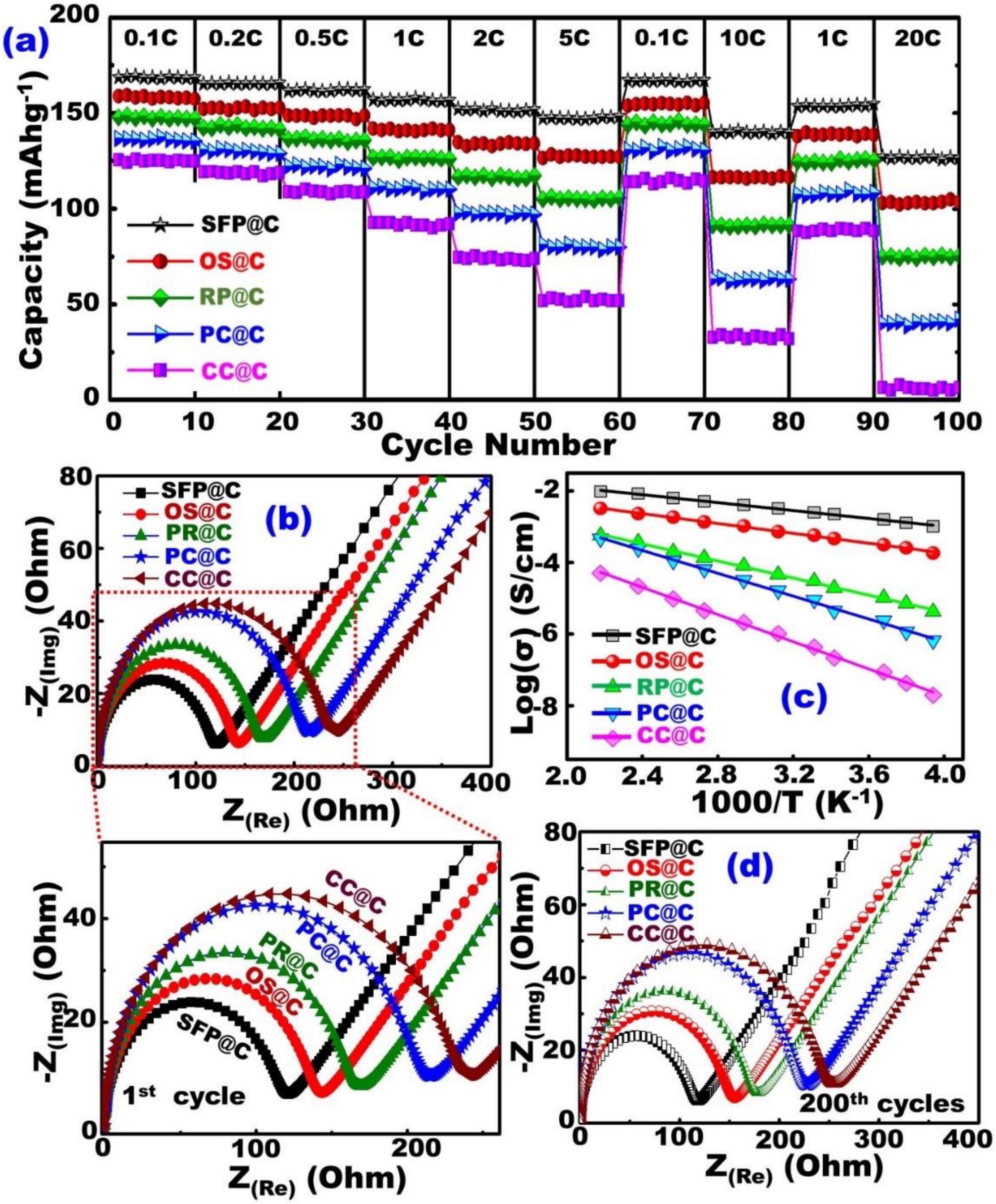

Fig. S11 Effect of variable model geometrics and multifaceted exposure sites of mesopolytopes SFP@C, OS@C, RP@C, PC@C, and CC@C half-cell cathodes on the electrochemical performance in terms of (a) Capability performance rates over a range of 2.0–4.3V at various current rates from 0.1C to 20C; **(b)** the electrochemical impedance spectroscopy (EIS) results; **(c)** Temperature dependence comparison of electrical conductivity; **(d)** the EIS results after 200 cycles. Among all mesopolytopes cathodes, the SFP@C cathode exhibits good conductivity and the high electron transport along tested temperature range (~250 to 455K). All electrochemical measurements for half-cell anodes were at room temperature.

S12. Electrochemical measurements of half-cell 1D-TO@C LIB-CR2032 coin-cells models

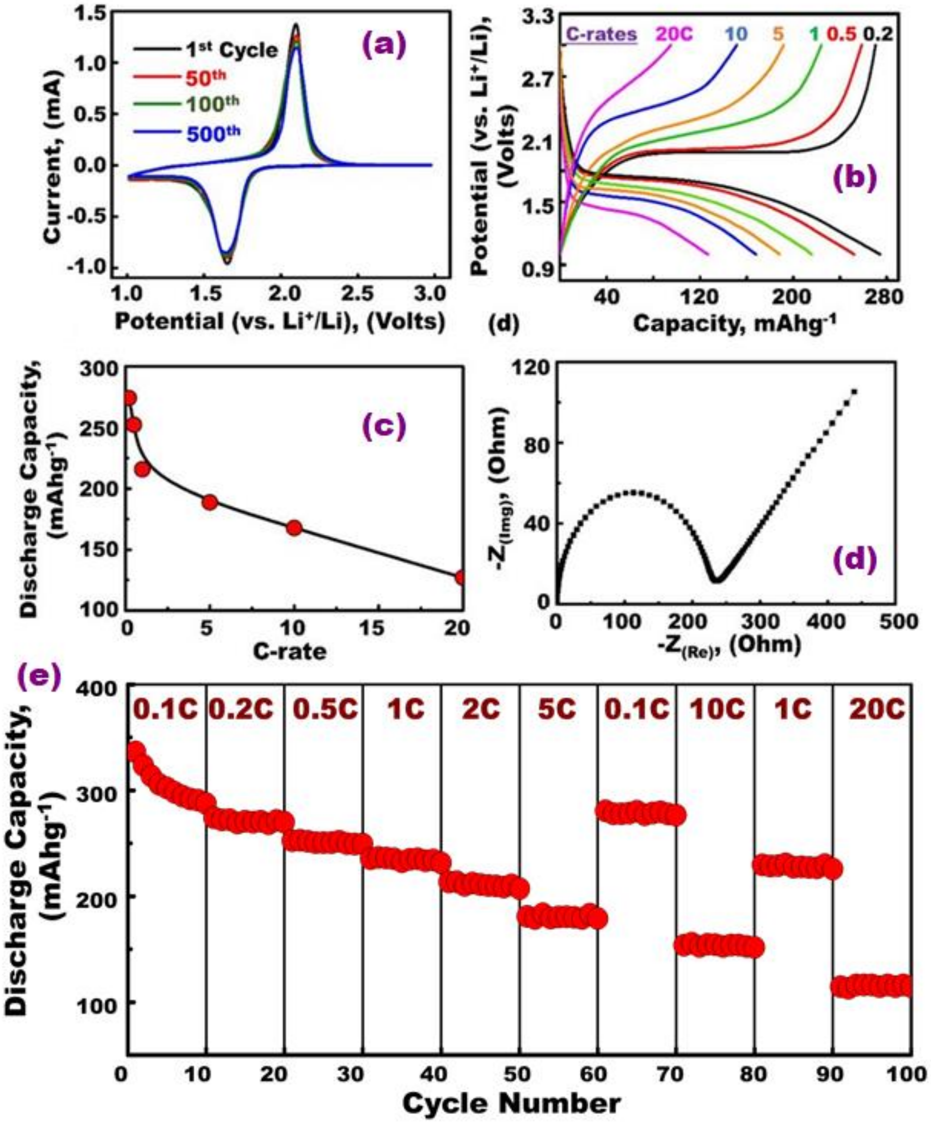

Fig. S12 **(a)** CV curves of half-cell 1D-TO@C anode LIB-CR2032 coin-cell models at different cycle numbers from 1st -500th cycles at 0.1 mVs^{-1}. **(b)** The charge-discharge voltage profiles of first cycle at multi-current rates 0.2C, 0.5C, 1C, 5C, 10C and 20C for half-cell TO@C anode material. **(c)** First discharge capacity of capsule 1D-TO@C anode N-electrode at current rates 0.2C -20C of half-cell LIBs. **(d)** The electrochemical impedance spectroscopy (EIS) results of capsule 1D-TO@C anode N-electrode in half-cell anode materials. All electrochemical measurements for half-cell TO@C anode material were operated within voltage range of (1.0-3.0 V), at 25 ºC. **(e)** Rate capability performance rates for half-scale 1D-TO@C capsule anode LIB-CR2032 coin-cells at various current rates from 0.1C to 20C.

S13. Key parameters of stacking layers of cell battery based pouch-type LIB models

The mass fraction components of formulated pouch-cell LIB models

The pouch LIB models are basically designed through a set of stacked layers of mesopolytope SFP@C cathode P-electrode // capsule 1D-TO@C anode N-electrode that oriented in full-scale LIB-CR2032-coin-cell components (Figure S13). The mass fraction of cathode as an individual component in a cell battery is approximately 43.8%, where the total cell mass equals 6 g (0.006 kg) see Figs. S13.

Per of our practical LIB-CR2032-coin cells, the mass composition ratio of active materials used in the working cathode electrode (SFP@C: carbon-black: PVDF linker) is 75: 15: 10. Then, the specific energy density of mesopolytope SFP@C // capsule 1D-TO@C LIB-CR2032-coin cells is practically equal to 186.98, and 177.81 Wh/kg at 0.1 C, and 1C, respectively for the SFP@C//TO@C full-scale LIBs (see below).

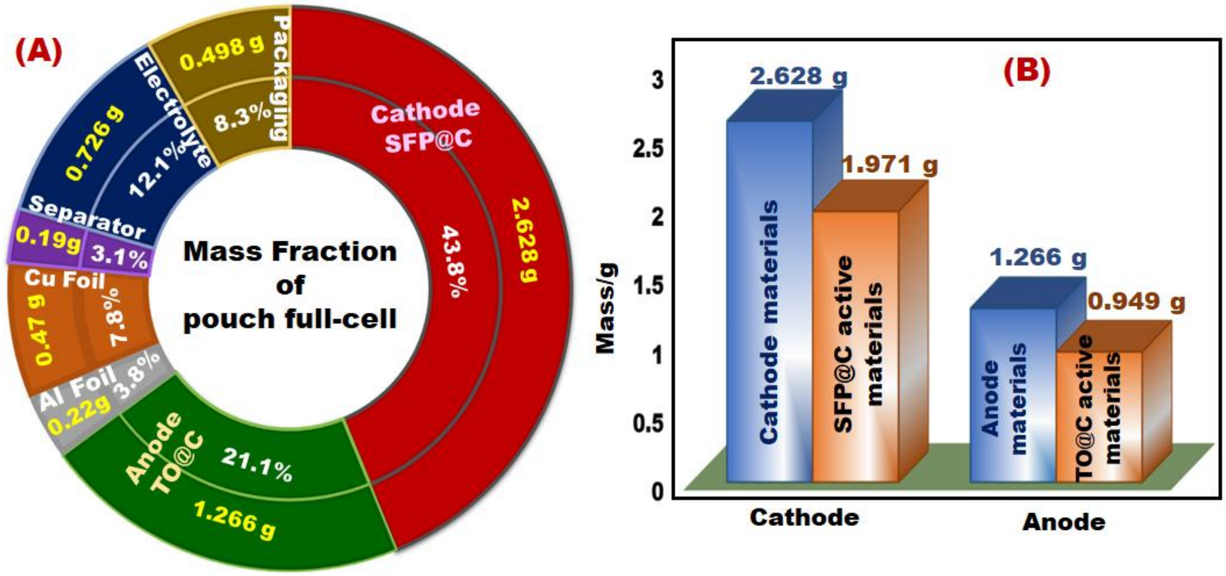

Fig. S13 Schematic diagram of the pouch cell model with its mass fraction of individual components used to control formation of stacking layers of mesopolytope SFP@C cathode P-electrode // capsule 1D-TO@C anode N-electrode into pouch LIB-model.

Mass balancing of P-, and N-electrodes in full-cell capacity ((.i.e., the balancing $(P/N)_{Cap}$ ratio)

The specific mass fraction value of P- and N-electrode materials presented in the mesopolytope SEP@C cathode P-electrode // capsule 1D-TO@C anode N-electrode in full-scale LIB-CR2032-coin-cells plays a major influence in controlling the cell capacity, energy density, and safety factors. In this key design of LIB-tradeoff configuration of the mesopolytope SEP@C cathode P-electrode // capsule 1D-TO@C anode N-electrode oriented in full-scale LIB-CR2032-coin-cells, we consider a control of the balancing $(P/N)_{Cap}$ ratio. The rational mass ratios of polytope SEP@C (P-electrode) and capsule 1D-TO@C (N-electrode) enable a reasonable control between these two contrast choices of (i) safety issue and (ii) preserving a high specific energy density. One of electrochemical properties firmly dependent of P/N proportion is the formation of lithium plating/deposition along anode surfaces during a charging procedure. To avoid the negative impact of lithium plating, which is largely a regressive aging and safety process, a slight increase in the overall mass loading capacity of the capsule 1D-TO@C anode (N-electrode) is required for both betterment safety and high specific energy storage [Ref-S7-S8]. It is necessary to maintain the balancing $(P/N)_{Cap}$ ratio ≈1.0: 1.07-1.14, as an optimal tradeoff relationship of our polytope SEP@C (P-electrode) and capsule 1D-TO@C (N-electrode) full cells (i.e., ensuring cell battery safety with production of high energy storage), according to the following key clues:

(i) To have cell battery safety betterment (i.e., which is practically controlled by increasing the mass loading of capsule 1D-TO@C (N-electrode), leading to $(P : N)_{Cap}$ ratio of $<1 : 1$), and

(ii) To keep the high specific energy storage (i.e., which is practically controlled at equal mass loading between the polytope SEP@C (P-electrode) and capsule 1D-TO@C (N-electrode), leading to equal capacities (i.e., $(P:N)_{Cap}$ ratio of 1:1).

Therefore, we fabricate polytope SEP@C cathode P-electrode // capsule 1D-TO@C anode N-electrode oriented in full-scale LIB-CR2032-coin-cells under optimizing $(P:N)_{Cap}$ ratio of ≈ 1.0: 1.09.

Specific energy density measurements of SFP@C //1D-TO@C full-scale CR2032-coin LIB cells

For the practical LIB-CR2032-coin cells, the mass composition ratios of active material components (i.e., SFP@C: carbon-black: PVDF of 75: 15: 10, respectively) play a role in the determination of the specific energy density. In galvanostatic charge-discharge test recorded at constant current and average voltage of 3.45V, one can determine the specific energy for the SFP@C cathode (Wh/kg) according to the following equation:

The specific energy density of SFP@C cathode P-electrode= the average working voltage (3.45 V) x maximum discharge capacity delivered at C-rates by half-cell cathode (Ah/kg) x active material % in total components.

Accordingly, at C-rate 0.1(mV/s);

The specific energy density of the SFP@C cathode (Wh/kg) = 3.45 * 165*0.75 =426.9 Wh/kg &

Accordingly, at C-rate 1.0 (mV/s);

The specific energy density of the SFP@C cathode (Wh/kg) = 3.45 *156.9 *0.75=405.97 Wh/kg.

The specific density energy for the mesopolytope SEP@C cathode P-electrode // capsule 1D-TO@C anode N-electrode in full-scale LIB-CR2032-coin-cells can be determined according to the following:

Considering the SFP@C cathode weight percentage of the full cell is 43.8 %, then one can consider as follows:

- ***(i) The specific energy density of the full cell LIBs at C-rate 0.1(mV/s) = 426.9*0.438= 186.98 Wh/kg.***
- ***(ii) The specific energy density of the full cell LIBs at C-rate 1.0 (mV/s) =426.9 * 0.438= 177.81 Wh/kg.***

S14. Areal discharge capacity and volumetric energy density of cell battery pouch LIB-models

To control design of the cell battery pouch LIB-models, mesopolytope SEP@C cathode P-electrode // capsule 1D-TO@C anode N-electrode stacked pouch LIB-model is designed with specific 3D dimensions of 35 mm (width), 55 mm (length) and ~2.5-3mm (thickness), respectively. The stacking sequence of P- and N-electrodes can be designed in well-packed and dense layers of TO@C-anode (5-layers/10-sides)//SFP@C-cathode (6-layers/10-sides) oriented in coin cells. In our large-scale, stacking-layer design configurations of pouch LIB-types, we consider the following key factors:

1. The mass component and fraction are determined along the pouch cell constitutes as shown in Figures S13.
2. The stacking-layer SFP@C (cathode) and TO@C (anode) design indicates that the actively-loaded mass of P-electrode cathode and N-electrode anode in the configurations of pouch LIB-types can be 1.97 g and 0.949 g; respectively.
3. Well-packed and dense layers TO@C-anode (5-layers/12-sides)//SFP@C-cathode (6-layers/12-sides) are contiguously connected into a series for configurations of pouch LIB-types.

In order to calculate the areal discharge capacity of pouch LIB designs, we optimize the electrode area of the full-cell mesopolytope SEP@C cathode P-electrode // capsule 1D-TO@C anode N-electrode LIBs by selection the following dimensions of (3*5=15 cm^2) and (3*4.75 = 14.3 cm^2) for SFP@C-cathode and 1D-TO@C-anode, respectively. Thus, the total area of the cathode and anode coverage the pouch LIB cells are 150 and 143 cm^2; respectively. Therefore, the mass stacking of mesopolytope SEP@C cathode P-electrode and capsule 1D-TO@C anode N-electrode is 13.14 and 6.63 mg/cm^2, respectively. Our finding indicates that the areal discharge capacity the stacking mesopolytope SEP@C cathode P-electrode and capsule 1D-TO@C anode N-electrode is 1.144 and 1.145 Ah/cm^2, respectively. The relatively similar values of areal discharge capacity of mesopolytope SEP@C cathode P-electrode and capsule 1D-TO@C anode N-electrode in the pouch LIB models indicate the following issues:

- ➢ the equal value of specific discharge capacity for mesopolytope SEP@C cathode P-electrode // capsule 1D-TO@C anode N-electrode, giving a real evidence of reasonable control of the $(P: N)_{Cap}$ capacity ratio = 1.0: 1.09, and
- ➢ the optimal tradeoff LIB manufacturing relationship between the safety betterment and the high specific energy density.

To calculate the volumetric energy density of pouch LIB designs, we formulated the full-scale LIB using stacked-layers of SEP@C cathode P-electrode // capsule 1D-TO@C anode N-electrode CR2032-coin cells oriented in pouch design. Therefore the calculation of volumetric energy density can be as follows:

- Volumetric energy density = gravimetric cell energy (Wh/kg)* total cell mass (kg)/ cell active area volume (L)
- However, gravimetric cell energy = 186.98 Wh/kg; total cell mass = 6 g = 0.006 kg; active area volume = 35 mm (width)* 55 mm (length)* 2.4 mm cell thickness = 4620 mm^3 = 0.00462 L

Then, the volumetric energy density =124.5 * 0.006 / 0.00462 = 242.83 Wh/L

S15. Stability of the mesopolytope cathode geometrics after multiple cycles

The effect of the multiple electrochemical charge/discharge cycling profiles after long-term 2000 cycles at rate of 1C on the morphological 3D LFPO@C cathode architects, for example, is investigated by using FE-SEM, and elemental mapping analysis images (EDS) Figure S14. The structural decomposition/degradation, to some extent, indicates the particular ageing of 3D LFPO@C centering components/sites after 2000 cycles of full-scale LIB comparing to pre-cycled LFPO@C electrodes, Figures (1, S2-S5). However, the outstanding stability of excellent electrochemical performance after 2000 cycles, the ~100% of Coulombic efficiency, high capacity at high rate capability, and long cycle life may be due to the maintenance of sustainable anode//cathode potentials. The following aspects are featured:

I. rapid electron movement reaction and Li^+-ion transportation kinetics along the mesopolytope crystal interfaces and facets during lithiation/delithiation processes;

II. multiple accommodation and storage space-like pockets along 1D and 3D meso/macrodiffusive open gates and channels, thereby enabling enable multiple directional electrons/Li^+ ion pathways, decrease in the distance of electron transport, high tap density, and multidiffusible Li^+ ions.;

III. a wide range of transport pathways of Li^+ ions along the 1D open-end directional gates of 1D TO@C nanorod capsules and 3D superscalable 3D-SFP@C crystal facets, thereby offering ageless, attainable LIBs with superb rate capability and long cycling stability;

IV. excellent electronic contact, electrical conductivity, and facile transport along sustainable mesopolytope SFP@C // capsule 1D-TO@C electrode surfaces; and

V. reduction of Li^+-ion diffusion paths/distances on cathode//anode surfaces during the lithiation/delithiation process.

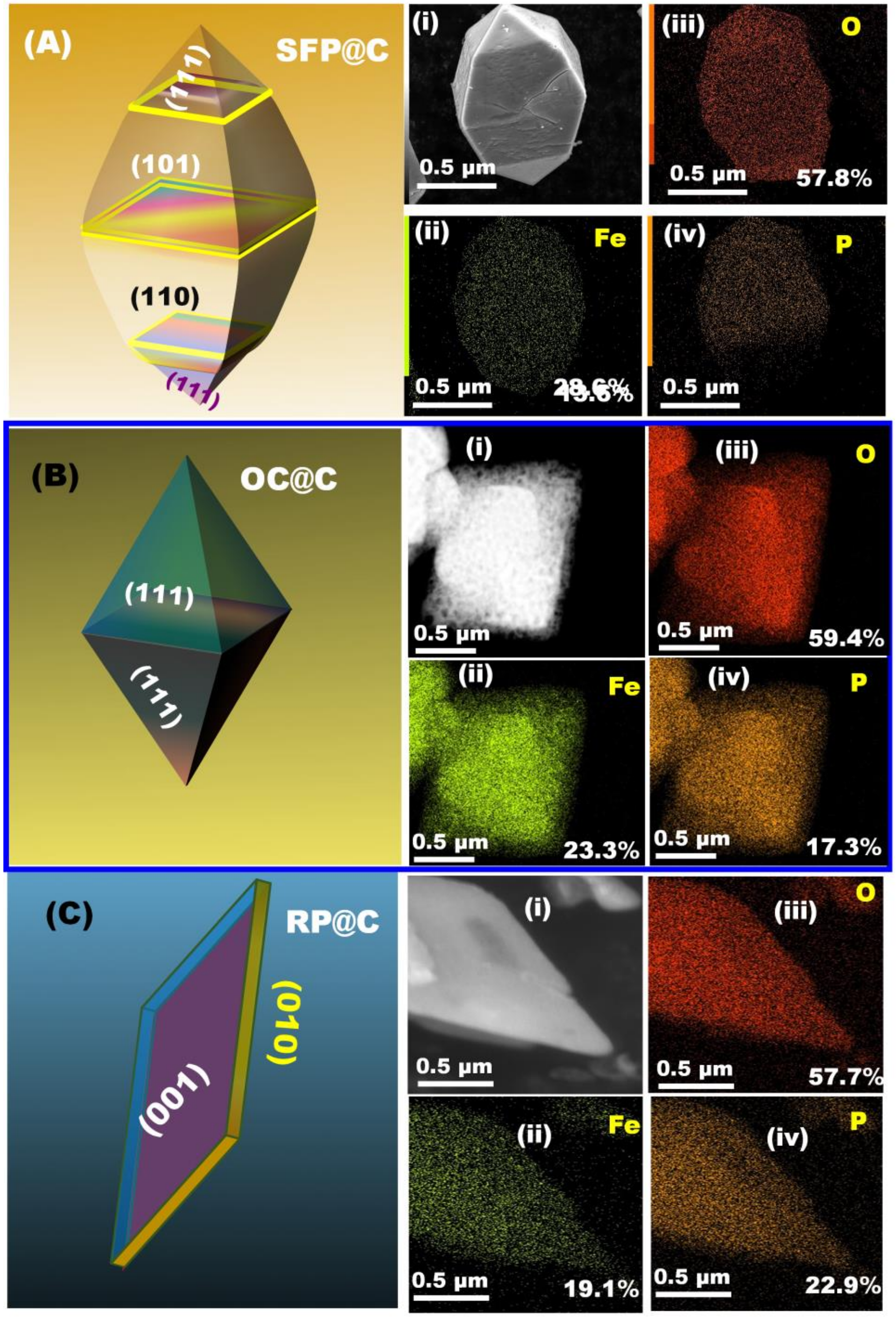

Fig. S14 FE-SEM, EDX-elemental mapping analysis of the different large-scale mesopolytope building blocks with heterogeneous high-index, homeomorphic sixteen-faceted exposure polyhedron SFP@C, OS@C, and RP@C mesopolytopes after long-term 2000 cycles at 1C. EDS elemental mapping analyses and images for SFP@C, OS@C, and RP@C, after long-term 2000 cycles at 1C (i-iv).

S16. Potential of full-cell mesopolytope SEP@C cathode P-electrode // capsule 1D-TO@C anode N-electrode LIBs with other designs

Table S1 A comparison between the full-cell mesopolytope SEP@C cathode P-electrode // capsule 1D-TO@C anode N-electrode LIBs and the other reported $LiFePO_4//TiO_2$ LIBs.

Cathode material	Anode material	Nominal Voltage (V)	Cycles	Specific Capacity mA h g^{-1}	Coulombic efficiency	Ref
$LiFePO_4$	TiO_2	1.5	retention of ~100% for 200 cycles	140	~100%	Ref [S1]
$LiFePO_4$	anatase/graphene	1.6	700	127	~ 100%	Ref [S2]
$LiFePO_4$@NC	spinel $Li_4Ti_5O_{12}$/rutile-TiO_2@C	1.8	retention of ~83.3% for 200 cycles	100.1		Ref [S3]
$LiFePO_4$	Anatase TiO_2 hollow nanofibers	1.4	retained 88% of its reversible capacity after 300 cycles	103	> 99 %	Ref [S4]
$LiFePO_4$	Rutile TiO_2	1.8	retained 50% of its reversible capacity after 40 cycles	150	Not mentioned	Ref [5]
$LiFePO_4$	Anatase TiO_2	1.6	81% of its initial capacity after 300 cycles at 20C	160	Not mentioned	Ref [S6]
$LiFePO_4$-C	TiO_2-C	1.5	retention of ~77% @ higher rate of 7.5 C	160	-	Ref [S7]
$LiFePO_4$	spinel $Li_4Ti_5O_{12}$/C	1.8	Retain 98.1% after 400 cycles	167	~100%	Ref [S8]
$LiFePO_4$	spinel $Li4Ti_5O_{12}$	1.65	Retain 98.9% after 100 cycles	150	~100%	Ref [S9]
3D-$LiFePO_4$@C	1D-TO@C	1.78	Retains 97.2% after 2000 cycles at 1C	176.9	~100%	Current Work

References:

[S1] Y. Nan, S. Li, B. Li, S. Yang, Nanoscale, **11** (2019), pp. 2194-2201

[S2] D. Choi, et al., Electrochem. Commun. **12(3)** (2010) pp. 378-381.

[S3] P. Wang, G. Zhang, J. Cheng, Y. You, Y.K. Li, C. Ding, J.J. Gu, X.S. Zheng, C.F. Zhang, F.F. Cao, ACS Appl. Mater. Interfaces **9(7)** (2017), pp. 6138-6143

[S4] X. Zhang, V. Aravindan, P. Suresh Kumar, H. Liu, J. Sundaramurthy, S. Ramakrishna, S. Madhavi Nanoscale, **5**, (2013) pp. 5973-5980.

[S5] J. Hassoun, M. Pfanzelt, P. Kubiak, M. Wohlfahrt-Mehrens, B. Scrosati, J. Power Sources, **217**, (2012) pp. 459-463

[S6] Z. Guo, X. Dong, D. Zhou, Y. Du, Y. Wang, Y. Xia, RSC Adv., **3** (2013) pp. 3352-3358.

[S7] F.F. Cao, X. L. Wu, S. Xin, Y.G. Guo, L.J. Wan, J. Phys. Chem. C **114(22)** (2010), pp.10308-10313

[S8] C-C.Yang, H-C. Hu, S.J. Lin, W-C. Chien, J. Power Sources, **258**, (2014) pp. 424-433.

[S9] J. Morales, R. Trocoli, S. Franger, J. Santos-Pena, Electrochim. Acta 55 (2010) pp. 3075e3082.